J. Fluid Mech. (2015), *vol.* 765, *pp.* 480–523.
doi:10.1017/jfm.2014.746

Experimental and theoretical study of wave–current turbulent boundary layers

Jing Yuan[1,†] **and Ole S. Madsen**[1]

[1]Department of Civil and Environmental Engineering, R. M. Parsons Laboratory, Massachusetts Institute of Technology, Cambridge, MA 02139, USA

(Received 9 September 2014; revised 19 November 2014; accepted 21 December 2014; first published online 28 January 2015)

An experimental study of turbulent wave–current boundary layer flows is performed using a state-of-the-art oscillating water tunnel (OWT) for flow generation and a particle image velocimetry system for velocity measurements. The current velocity profiles in the presence of sinusoidal waves indicate a two-log-profile structure suggested by the widely-used Grant–Madsen model. However, for weak currents in the presence of nonlinear waves, the two-log-profile structure is contaminated or even totally obliterated by the boundary layer streaming which is produced by the asymmetry of turbulence in successive half-periods of nonlinear waves. To interpret experimental results, a semi-analytical model which adopts a rigorous way to account for a time-varying turbulent eddy viscosity is developed. The model can accurately predict turbulence asymmetry streaming, which leads to successful predictions of the mean velocity embedded in nonlinear-wave tests and the current velocity profiles in the presence of either sinusoidal or nonlinear waves. Since the Longuet-Higgins-type streaming due to wave propagation is absent in OWT flows and not included in the semi-analytical model, future work is necessary to extend this study for applications in the coastal environment.

Key words: boundary layers, coastal engineering, sediment transport

1. Introduction

In the coastal environment, surface waves and currents are always simultaneously present and nonlinearly interact with each other in the near-bottom region, which leads to a wave–current boundary layer. A thorough understanding of this combined wave–current boundary layer is a prerequisite for the prediction of currents, i.e. circulation, as well as sediment transport in coastal waters, as evidenced by the large number of studies on this topic over the past decades. For typical coastal wave–current flows, the wave boundary layer is usually much thinner than the current boundary layer, e.g. the boundary layer of storm-produced surface waves is only a few centimetres thick, while the current boundary layer can occupy the entire water depth (several metres). Therefore, in the immediate vicinity of the bottom, the flow is controlled by turbulence

† Present address: Department of Civil and Environmental Engineering, National University of Singapore, Singapore 117576, Singapore.
Email address for correspondence: ceeyuan@nus.edu.sg

produced by both waves and currents, but at higher elevations the flow only feels the turbulence produced by currents since the wave boundary layer vanishes quickly with elevation. Based on this concept, Grant & Madsen (1979) proposed a time-invariant two-layer turbulent eddy viscosity model to analytically solve the linearized horizontal momentum equation. In their model, the turbulent eddy viscosity is scaled with the combined maximum shear velocity within the wave boundary layer, but is scaled with the current shear velocity outside the wave boundary layer. They showed that currents are significantly retarded by co-existing waves, which can be conceptualized by a large apparent roughness experienced by a current in the presence of waves. This is of significant importance for modelling nearshore circulations, and the model's validity is supported by many field (e.g. Drake & Cacchione 1992) and laboratory (e.g. Mathisen & Madsen 1996*b*) measurements. Following the same concept, there are many other analytical models based on different formulations of a time-invariant turbulent eddy viscosity, e.g. Dungan Smith (1977), Christoffersen & Jonsson (1985), Myrhaug & Slaattelid (1989) and Sleath (1991).

Other than this basic wave–current interaction, waves also create a boundary layer streaming that is added to the co-existing currents. In coastal regions the spatial inhomogeneity due to surface wave propagation leads to a small vertical velocity within the bottom boundary layer. The vertical and horizontal velocities are not completely 90° out of phase, so the convective terms in the horizontal momentum equation have non-zero period-averaged values, producing a mean horizontal velocity (referred to as progressive wave streaming or PW-streaming hereafter). Longuet-Higgins (1953) first analytically explained this phenomenon for laminar flows and showed that the streaming is in the wave direction. In the appendix to Russell & Osorio (1958), he demonstrated that if turbulence within the wave boundary layer is modeled with a time-invariant eddy viscosity the conclusions for laminar flows are also applicable for turbulent flows.

Waves become increasingly nonlinear as they propagate toward the shoreline, so the time series of the near-bottom flow over a wave period is skewed (peaked crest and flat trough) and has forward-leaning crests, creating asymmetry of turbulence in successive half-periods of nonlinear waves. This is another mechanism that produces a mean horizontal velocity (referred to as turbulence asymmetry streaming or TA-streaming hereafter). Trowbridge & Madsen (1984*a*,*b*) developed an analytical model for progressive nonlinear waves based on a time-varying turbulent eddy viscosity. In their model a small first-harmonic turbulent eddy viscosity, arising from the turbulence asymmetry, interacts with the dominant first-harmonic velocity to produce a boundary layer streaming that is in the opposite direction to wave propagation. Similar results are obtained in many numerical studies based on the linearized wave boundary layer equation (e.g. Davies & Li 1997; Holmedal & Myrhaug 2006; Scandura 2007; Fuhrman, Fredsøe & Sumer 2009), which is not surprising since numerical turbulent closure schemes automatically account for a time-varying turbulent eddy viscosity.

Given their opposite directions, the TA-streaming competes with the PW-streaming. Holmedal & Myrhaug (2009), Blondeaux *et al.* (2012) and Kranenburg *et al.* (2012), among others, used numerical models to study the co-existence of the two kinds of boundary layer streaming. Their results confirm the conclusion by Trowbridge & Madsen (1984*b*) that the relative importance of one streaming over the other depends on wave characteristics and bottom roughness conditions. Because the Grant–Madsen model assumes a horizontally uniform flow and a time-invariant turbulent eddy viscosity, boundary layer streaming is completely absent in their basic wave–current

model, and hence can be considered another effect of wave–current interaction. Gonzalez-Rodriguez & Madsen (2011) extended the analytical model of Trowbridge & Madsen (1984*b*) to waves plus weak currents, but their model does not outperform the Grant–Madsen model for currents in the presence of collinear sinusoidal waves. Holmedal, Johari & Myrhaug (2013) numerically studied the effects of both PW- and TA-streamings on the basic wave–current interaction, but were unable to validate their numerical results due to the lack of suitable experimental evidence.

Most previous experimental studies on wave–current boundary layers were performed in laboratory wave flumes or wave basins. In wave flumes waves and currents are collinear, but in real coastal waters they are usually close to orthogonal. Nevertheless, flume experiments provide valuable measurements for understanding the fundamentals of wave–current interaction (e.g. van Doorn 1981; Kemp & Simons 1982, 1983; Mathisen & Madsen 1996*a*,*b*, 1999; Fredsøe, Andersen & Sumer 1999). To account for various angles between waves and currents, a limited number of experiments have been conducted in wave basins (e.g. Bijker 1966; Arnskov, Fredsøe & Sumer 1993; Musumeci *et al.* 2006; Fernando, Guo & Lin 2011; Lim, Madsen & Cheong 2012).

A major problem with these two types of facilities is their inability to produce prototype flow conditions. Dimensional analysis suggests that wave boundary layers are controlled by two dimensionless parameters: the amplitude Reynolds number $Re = A_{bm}U_{bm}/\nu$ and the relative roughness A_{bm}/k_b, where U_{bm} is the near-bottom wave orbital velocity amplitude, A_{bm} is the near-bottom excursion amplitude, ν is the molecular kinematic viscosity of the fluid and k_b is the bottom roughness. For a surface wave which can induce noticeable amounts of sediment transport Re and A_{bm}/k_b can be up to $O(10^6)$ and $O(10^3)$, respectively. Such high values cannot be achieved in regular laboratory wave flumes or wave basins due to their physical limitations. Therefore, another type of facility, oscillating water tunnels (OWT), has been employed for full-scale experimental studies.

OWTs are usually U-shaped enclosed tunnels with a piston located at one end producing oscillatory motions. It should be noted that boundary layer flows in OWTs are uniform along the horizontal direction, so they do not exactly mimic those under progressive waves, i.e. they reproduce the TA-streaming but miss the PW-streaming entirely. However, this drawback makes OWT experiments perfect for validating theoretical models based on the linearized boundary layer equations, e.g. the Grant–Madsen model. Initially, OWTs were used for studying sinusoidal wave boundary layers, e.g. Jonsson & Carlsen (1976), Sleath (1987) and Jensen, Sumer & Fredsøe (1989). There are also a few experiments corresponding to nonlinear waves, e.g. Ribberink & Al-Salem (1995) and van der A *et al.* (2011) who observed negative (against the wave direction) boundary layer streaming embedded in two types of nonlinear waves, Stokes second-order waves and forward-leaning waves, respectively. These observations directly demonstrate the existence of the TA-streaming, since the PW-streaming does not exist in OWTs. Only a small number of experimental studies on combined wave–current flows in OWTs have been reported. Lodahl, Sumer & Fredsøe (1998) studied combined wave–current flows in smooth pipes placed in an OWT, Dohmen-Janssen (1999) measured turbulent wave–current boundary layers over both fixed and movable sediment-covered bottoms, while Wijetunge (2006) considered a fixed rippled bed. All these studies are based on sinusoidal waves. To the authors' knowledge, no experiment on nonlinear waves plus currents in OWTs has been reported to date.

Generally speaking, there is still an urgent need for more experimental data on wave–current boundary layers, especially for experiments with a well-known

physical bottom roughness. Since OWTs provide the most controllable experimental conditions, it is therefore necessary to continue using such facilities to produce more experimental results, even though the PW-streaming is excluded. Thus, in this study we conduct a comprehensive experimental study of wave–current boundary layers using a newly-built OWT for flow generation and a state-of-the-art particle image velocimetry (PIV) system for velocity measurements. Tests are performed for both sinusoidal and nonlinear waves combined with collinear currents. We also perform tests over three different fixed bottom configurations with well-understood physical bottom roughness. Following Gonzalez-Rodriguez & Madsen (2011), we develop a theoretical model based on the linearized boundary layer equation and a time-varying turbulent eddy viscosity to interpret our experimental results. With this theoretical model, the effect of TA-streaming on wave–current interaction in OWTs is quantitatively discussed. The experimental setup is introduced in § 2, and some experimental results are presented in § 3. The theoretical model is outlined in § 4 and validated against experimental results in § 5.

2. Experimental setup

2.1. *Experimental facility*

The experimental facility is a newly-built OWT, named the wave–current–sediment facility (WCS), in the Hydraulic Engineering Laboratory of the Department of Civil and Environmental Engineering at the National University of Singapore. The facility has a 10 m long, 50 cm deep and 40 cm wide horizontal test channel and a powerful piston system which can generate a variety of periodic oscillations corresponding to full-scale flow conditions along the entire test channel. These oscillatory flows in the WCS will be simply referred to as 'waves' hereafter. A Börger EL1550 Rotary Lobe pump is connected to introduce collinear currents of up to 60 cm s^{-1} average velocity in the test channel. The current direction can be easily reversed by reversing the pump's rotation. A two-dimensional PIV system, supplied by the TSI Corporation, is used to obtain velocity measurements. For most tests in this study, the vertical resolution is approximately 0.4 mm/grid, which is sufficiently fine to reveal details of the boundary layer flows. Each measurement is obtained over N wave periods, and the velocities measured at the same vertical level at M different longitudinal positions, x_m, are effectively homogeneous, so the Reynolds-averaged velocity profiles over a wave period are obtained by performing both spatial and phase averaging:

$$\langle\hat{\xi}\rangle(z,t)=\frac{1}{MN}\sum_{m=1}^{M}\sum_{n=1}^{N}\xi(x_m,z,t+(n-1)T),\quad 0<t<T \tag{2.1}$$

where ξ is either the horizontal or vertical component of flow velocity (u, w), t is the time, and (x_m, z) are the horizontal and vertical coordinates. In the following we will, unless otherwise indicated, for simplicity use $\xi(z, t)$ to denote the double-averaged quantities. The reader is referred to Yuan & Madsen (2014) (YM14 hereafter) for more details on the WCS and the PIV system.

2.2. *Bottom conditions*

In this study, three bottom conditions, a smooth bottom and two fixed rough bottoms, are included. The smooth bottom is formed by smooth aluminium plates. One fixed rough bottom is created by gluing 3M^{TM} 710 Safety-WalkTM Slip-Resistant Coarse

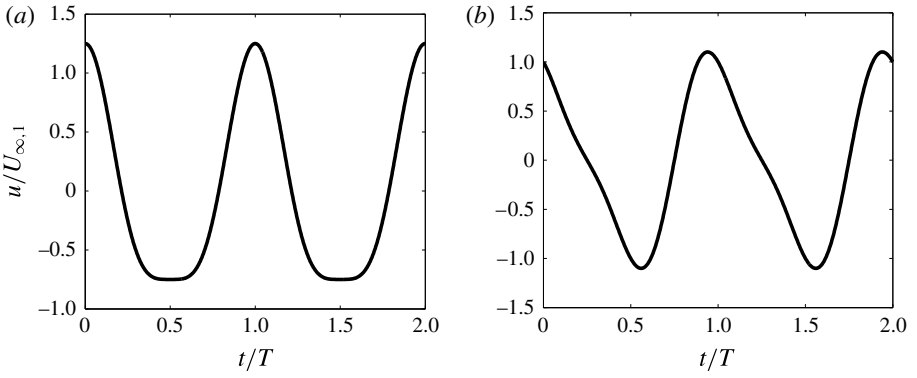

FIGURE 1. Free-stream velocities of nonlinear waves: (*a*) Stokes wave; (*b*) forward-leaning wave.

tapes (physical roughness scale of approximately 1 mm) onto the aluminium plates. This bottom will hereafter be referred to as the 'sandpaper' bottom. The other rough bottom consists of a mono-layer of 12.5 mm-diameter ceramic marbles glued onto aluminium plates.

The theoretical bottom location $z = 0$ and bottom roughness k_b were determined by YM14 for each bottom condition by logarithmic profile fitting the near-bottom velocity measurements for several pure current and pure sinusoidal wave tests. For the smooth bottom, $z = 0$ is directly determined from the PIV images with only 0.1 mm uncertainty, and the effective bottom roughness formula for steady turbulent flows in smooth pipes by Nikuradse (1932), $k_b = 3.3\nu/u_*$, is found also to be applicable for smooth turbulent oscillatory flows if the period-averaged magnitude of shear velocity u_* is used as the characteristic shear velocity. For the sandpaper bottom, $z = 0$ is found to be 0.6 mm $\pm$ 0.1 mm below the mean crest level of bottom roughness elements and the Nikuradse equivalent sand grain roughness k_N is 3.7 mm $\pm$ 0.1 mm. For the ceramic-marble bottom, $z = 0$ is 4.0 mm $\pm$ 0.4 mm (roughly 1/3 of the ceramic marbles' diameter) below the top of the marbles and k_N is 20 mm $\pm$ 3 mm. For further details on the determination of the bottom conditions summarized above, including the log-profile fitting analysis, the reader is referred to YM14.

2.3. *Flow conditions*

Three periodic wave shapes, sinusoidal, Stokes and forward-leaning waves, are included in this study. The latter two are the sum of two harmonics:

$$u_\infty(t) = U_{\infty,1}\cos(\omega t) + \frac{U_{\infty,1}}{4}\cos(2\omega t + \varphi_{\infty,2}). \tag{2.2}$$

The second-harmonic phase $\varphi_{\infty,2}$ is 0° for Stokes waves and 90° for forward-leaning waves. As shown in figure 1, they represent the skewed and forward-leaning nature of near-bottom flows under nonlinear waves, respectively. For each wave shape, a variety of wave amplitudes and two wave periods (6.25 and 12.5 s) are considered, as summarized in table 1. Here the amplitudes are controlled by the first-harmonic displacement amplitude of the piston s_1, so the measured $U_{\infty,1}$ may deviate slightly (1–5 %) from the nominal values listed in the fourth column of table 1 which are the

Test ID	Wave shape	s_1 (mm)	Approx. $U_{\infty,1}$ (cm s^{-1})	T (s)	Re ($\times 10^6$)
SP400a	Sinusoidal	400	157.9	6.25	3.1
SP400b	Sinusoidal	400	79.0	12.5	1.6
SP250	Sinusoidal	250	98.7	6.25	1.2
SP200	Sinusoidal	200	39.5	12.5	0.4
ST400a	Stokes	400	157.9	6.25	3.1
ST400b	Stokes	400	79.0	12.5	1.6
ST200	Stokes	200	79.0	6.25	0.4
FL320a	Forward-leaning	320	126.3	6.25	2.1
FL320b	Forward-leaning	320	63.2	12.5	1.1
FL160	Forward-leaning	160	63.2	6.25	0.5

TABLE 1. Target wave conditions (s_1: first-harmonic displacement amplitude of the piston; $U_{\infty,1}$: approximate amplitude of the first-harmonic free-stream velocity; T: wave period; $Re = U_{\infty,1}A_{\infty,1}/\nu$: Reynolds number based on first-harmonic free-stream velocity).

cross-section averaged $U_{\infty,1}$ based on s_1. The PIV sampling frequency is 5.12 Hz for all tests, so the number of samplings per period is 32 for the short-period (6.25 s) tests and 64 for the long-period (12.5 s) tests. Each test is sampled for 32 wave periods, which was determined to produce reliable phase averaging. Current generation is specified by the pump's working frequencies f. Higher working frequency gives stronger current. Two currents for which the pump's frequencies are 13 and 40 Hz are considered in this study. For various wave conditions the ratio of current bottom shear stress τ_{cb} to maximum wave bottom shear stress τ_{wm} varies between 8 % and 60 %. This range should be sufficient to cover most wave–current flows encountered in the coastal environment. Since the nonlinear waves have direction dependence, currents in both positive and negative directions are considered. Here the positive direction is the direction of positive wave velocity, e.g. the direction of the maximum velocity of Stokes waves.

A three-part scheme, 'wave_current_bottom', is used to identify tests: 'wave' is the wave identifier chosen from the test IDs listed in table 1; 'current' is the current identifier in the form of 'C' plus a number indicating f, e.g. C13 denotes a current with a 13 Hz pump frequency. For currents in the negative direction, a letter 'r' (for 'reverse') is added to the identifier, e.g. 'C13r'. Finally 'bottom' is the bottom identifier which is chosen from 'sm' (the smooth bottom), 'sa' (the 'sandpaper' bottom) and 'ce' (the ceramic-marble bottom). For example, the test ST400a_C40r_ce is a combination of the Stokes wave given by the fifth row in table 1 and a 40 Hz current in the negative direction over the ceramic-marble bottom.

2.4. *Evaluation of current generation*

YM14 showed that the WCS can generate a desired wave motion with excellent accuracy, i.e. the amplitude of the oscillatory velocity is produced within 1 % of the target value, so here only the evaluation of current generation is presented.

To check the pump's ability to generate steady discharges when operating alone, five preliminary current-only tests for which the pump's working frequencies are 13, 26, 40, −26 and −40 Hz are performed over the sandpaper bottom (minus signs indicates reversed rotation). The current velocity profiles within 10 cm from the bottom are measured using the PIV system with a 5 Hz sampling frequency. Figure 2(*a*) shows

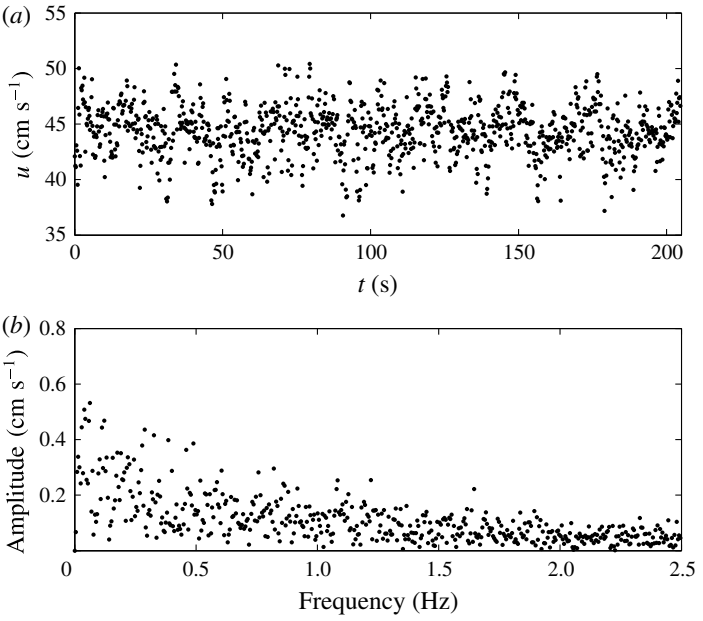

FIGURE 2. Spatial-average velocity of 40 Hz test measured at 90 mm above the sandpaper bottom: (*a*) time series; (*b*) frequency spectrum.

the spatial-averaged velocity of the 40 Hz test measured at 90 mm above the bottom. The time series shows no visually detectable trend of variation over the entire test duration. The random fluctuation gives a standard deviation of 2.0 cm s^{-1} which is less than 5 % of the mean value (44.3 cm s^{-1}). It is due to the residual turbulence after spatial averaging and the pulsating nature of the rotary lobe pump's current generation. The frequency spectrum shown in figure 2(*b*) suggests that this random fluctuation is spread over the entire resolvable frequency range (0–2.5 Hz). For typical wave–current flows with over 1 m s^{-1} wave velocity amplitudes and 0.1–0.5 Hz wave frequency, such noise (generally less than 0.2 cm s^{-1} in amplitude) will add less than 1 % error to the measured wave velocity. Thus, it should not be a concern for either current generation or wave velocity measurements.

The total pump discharge should be proportional to the pump's rotation frequency. Here the current velocity measured at 250 mm/2.72 = 90 mm above the bottom is used as a rough estimate of the cross-section average velocity by assuming that (*a*) the cross-section average velocity is close to the depth-average velocity of the bottom boundary layer, (*b*) the bottom boundary layer thickness is half of the channel working depth (250 mm) and (*c*) the current velocity profile within the bottom boundary layer is logarithmic. The measurements are plotted against the pump rotation frequency f in figure 3. The signs of reversed currents are changed for easy comparison. Clearly, the measurements fall nicely on a fitted straight line giving a slope of 1.14 cm s^{-1} Hz with a ±8 % 95 %-confidence interval:

$$\bar{u}_c\ (\text{cm s}^{-1}) = 1.14 f\ (\text{Hz}). \tag{2.3}$$

Thus, the average current velocity nominal magnitude is accurately determined from the pump rotation frequency.

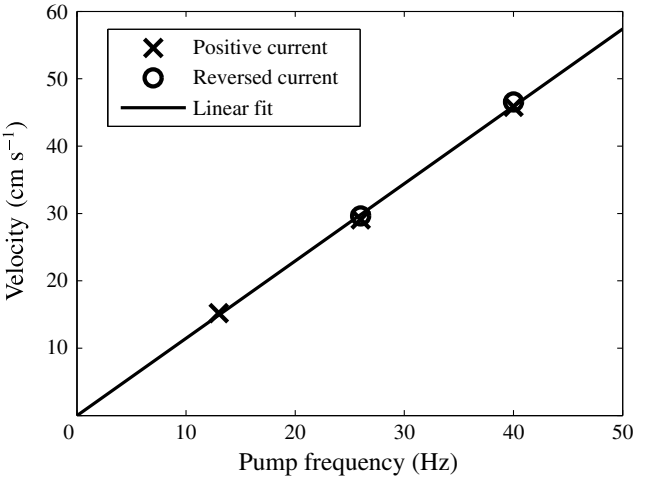

FIGURE 3. Cross-section average current velocities under different pump rotation frequencies, showing current in the positive and negative directions and a linear fit).

For current generation, the most important requirement is its stability, i.e. the pump must be able to produce a steady discharge against the time-varying pressure produced by the piston oscillatory motion. This can be demonstrated if (*a*) no sizeable harmonics other than the intended harmonics exist in the frequency spectrum of free-stream velocity and (*b*) the generation of intended harmonics is as excellent as when waves are generated alone. To evaluate the extent to which our current-generation system meets these requirements, two preliminary tests of combined wave–current flows and a baseline pure wave test over the sandpaper bottom were performed. In the three tests, the piston produces a SP400a wave, sinusoidal oscillation with approximately 160 cm s^{-1} first-harmonic free-stream velocity amplitude and 6.25 s period, while the pump rotation frequencies are 13 and 40 Hz for the two wave–current tests.

To evaluate our current-generation system performance, we should consider the flow velocity within the free-stream region of the wave boundary layer, so the spatial-averaged but not phase-averaged measurements at 17 cm above the bottom are selected in the following analysis. Figure 4 shows the frequency spectrum of the measurements for test SP400a_C40_sa. For clarity, the frequency is normalized by the wave frequency (0.16 Hz). The intended first-harmonic velocity and the mean (current) velocity are obviously much larger than any other harmonic. The residual noise (mostly less than 0.4 cm s^{-1}) is comparable to the noise in figure 2(*b*). Some integer-number harmonics, indicated by the circles, e.g. the second and third harmonics, are much larger than the residual noise but much smaller than the intended first harmonic. These higher harmonics are most likely produced by boundary layer processes related to the temporal variation of the turbulent eddy viscosity as discussed by YM14. Therefore, no unwanted harmonics in the frequency spectrum are produced by current generation. The first three harmonics of the measured free-stream velocity are shown in table 2. The free-stream velocity can also be inferred from the measured piston displacements based on continuity, and the results (denoted by 'inferred') are listed together with PIV measurements in table 2 for comparison. The excellent agreement among the three inferred first-harmonic amplitudes ($U_{\infty,1}$) suggests that

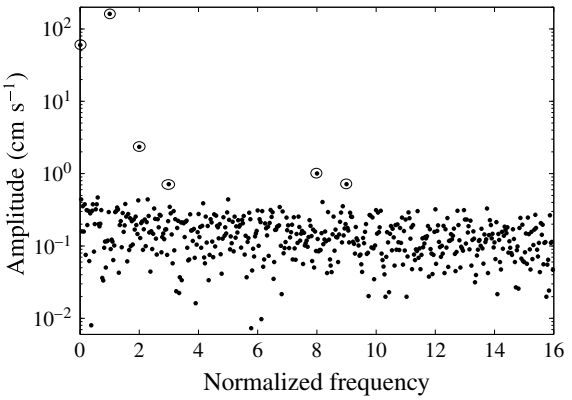

FIGURE 4. Frequency spectrum of spatial-averaged free-stream velocity of test SP400a_C40_sa (frequency is normalized by the wave frequency 0.16 Hz).

	$U_{\infty,1}$ (cm s^{-1})		$U_{\infty,2}$ (cm s^{-1})		$U_{\infty,3}$ (cm s^{-1})	
	Inferred	PIV	Inferred	PIV	Inferred	PIV
SP400a	161.28	160.71	0.28	1.49	1.25	0.23
SP400a_C13_sa	161.52	161.71	0.51	1.67	1.35	0.29
SP400a_C40_sa	161.24	161.54	0.92	2.36	1.26	0.75

TABLE 2. Comparison of measured free-stream velocity to the free-stream velocity inferred from piston displacement measurements ($U_{\infty,1}$, $U_{\infty,2}$ and $U_{\infty,3}$ are the amplitudes of the first three harmonics).

the piston oscillatory movement is not affected by current generation. The $U_{\infty,1}$ of wave–current tests deviate from the inferred values by only 0.2–0.3 cm s^{-1} (0.2 % of $U_{\infty,1}$), which is similar to wave-alone tests reported by YM14. The PIV measured second and third harmonics ($U_{\infty,2}$ and $U_{\infty,3}$) are affected by boundary layer processes and therefore not in agreement with the inferred values, but they are not intended to exist and are sufficiently small to be considered negligible. These results, together with the fact that no unwanted harmonics are observed, demonstrate excellent stability of the current-generation system.

3. Experimental results

Experimental results for currents in the presence of sinusoidal and nonlinear waves are discussed separately in this section. For each test, the Reynolds-averaged velocity profiles obtained from analysing PIV measurements are period-averaged to give a current velocity profile and Fourier analysed to give significant harmonics of the oscillatory velocity.

3.1. *Sinusoidal-wave–current boundary layers*

3.1.1. *Velocity profiles*

The basic wave–current interaction illustrated by the Grant & Madsen (1979) model (GM hereafter) is ideal for describing the sinusoidal-wave–current flows in OWTs. In the GM model, the following two-layer time-invariant turbulent eddy viscosity ν_t is

proposed:

$$\nu_t = \begin{cases} \kappa u_{*m} z, & z \leqslant \delta_{cw}, \\ \kappa u_{*c} z, & z > \delta_{cw}, \end{cases} \tag{3.1}$$

where u_{*c} is the current shear velocity $\sqrt{\tau_{cb}/\rho}$, u_{*m} is the maximum shear velocity $\sqrt{\tau_{bm}/\rho}$, δ_{cw} is a transition level where wave-produced turbulence vanishes and κ is the von Kármán constant which is found to be between 0.38–0.42 in various studies (we simply use 0.40 hereafter). Here τ_{cb} and τ_{bm} are the current and maximum combined wave–current bottom shear stresses, respectively. The vertical variation of the current shear stress τ_c is neglected by assuming the region of interest is the very near-bottom part of the entire current boundary layer, so the linearized boundary layer equation is solved analytically to give a two-log-profile structure for the current velocity profile:

$$\bar{u} = \begin{cases} \dfrac{u_{*c}^2}{\kappa u_{*m}} \ln\left(\dfrac{z}{z_0}\right) = \dfrac{\alpha u_{*c}}{\kappa} \ln\left(\dfrac{z}{z_0}\right) = \dfrac{u_{*c,1}}{\kappa} \ln\left(\dfrac{z}{z_0}\right), & z \leqslant \delta_{cw}, \\ \dfrac{u_{*c}}{\kappa} \ln\left(\dfrac{z}{z_{0a}}\right) = \dfrac{u_{*c,2}}{\kappa} \ln\left(\dfrac{z}{z_{0a}}\right), & z > \delta_{cw}, \end{cases} \tag{3.2}$$

where $\alpha = u_{*c}/u_{*m}$ and z_{0a} defines a new roughness scale $k_a = 30 z_{0a}$, the apparent roughness. If waves are present, z_{0a} is always larger than $z_0 = k_b/30$, sometimes by several orders of magnitude, which means that the current velocity profile, except for the very near-bottom region, experiences a dramatically increased apparent bottom roughness. The only influence of currents on waves is a slight increase of the turbulent eddy viscosity due to τ_{cb}, so waves effectively do not feel the existence of currents. The model prediction suggests that the amplitude of the first-harmonic velocity U_1 follows a logarithmic profile controlled by z_0 in the very near-bottom region:

$$U_1 = \frac{u_{*wm}^2}{\kappa u_{*m}} \ln\left(\frac{z}{z_0}\right) = \frac{u_{*w,1}}{\kappa} \ln\left(\frac{z}{z_0}\right), \tag{3.3}$$

where u_{*wm} is the maximum wave shear velocity $\sqrt{\tau_{wm}/\rho}$ with τ_{wm} being the maximum wave bottom shear stress. The predictive abilities of the original GM model are not always satisfactory due to some oversimplifications, e.g. the proposed discontinuous two-layer structure is only conceptually correct, so it was further modified several times (e.g. Madsen 1994). Humbyrd (2012) provided the latest and most consistent modification based on a continuous three-layer structure for ν_t (see appendix A for details). Therefore, we shall use it for quantitative comparisons with our measurements and hence name it the 'improved GM model'.

Figure 5 shows the measured current velocity profile and the amplitude profile of the first-harmonic velocity for a typical test over the ceramic-marble bottom, SP400a_C40_ce. This test has a sinusoidal wave of approximately 160 cm s^{-1} free-stream velocity amplitude with 6.25 s period and a cross-section average current velocity of approximately 46 cm s^{-1}. The current velocity profile clearly exhibits the two-log-profile structure suggested by the GM model. The lower current profile has a relatively larger slope, which indicates that it is scaled by a reduced shear velocity, i.e. $\alpha = u_{*c}/u_{*m} < 1$ in (3.2). The amplitude profile of the first-harmonic velocity can be well represented by a straight line in the very near-bottom region, which is in agreement with (3.3).

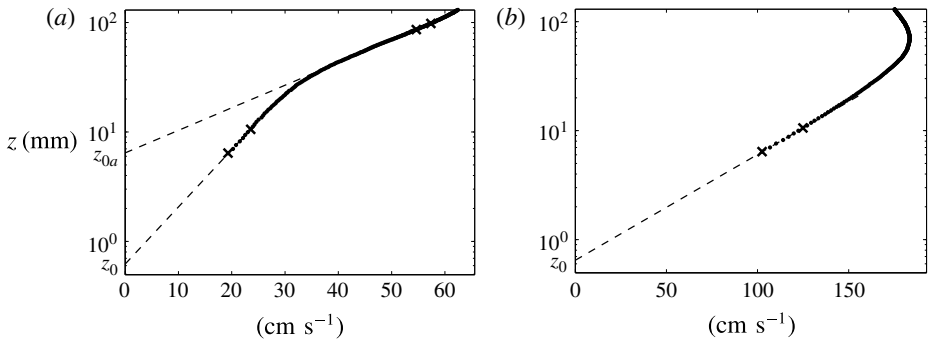

FIGURE 5. Velocity profiles of test SP400a_C40_ce: (*a*) current velocity profile; (*b*) first-harmonic amplitude profile (dots: measurements; dashed lines: fitted logarithmic profiles; crosses: limits for selecting data points for log-profile fitting).

The following data selection rules are applied to select measurements for log-profile fittings. According to Grant & Madsen (1979), the first-harmonic velocity amplitude profile is logarithmic in the very near-bottom region. Therefore, to fit the first-harmonic velocity amplitude profile and the lower current velocity profile which is supposed to be within the wave boundary layer, an upper data selection limit is imposed:

$$z/l < 0.15 \tag{3.4}$$

where the characteristic wave boundary layer length scale l is

$$l = \frac{\kappa u_{*m}}{\omega}. \tag{3.5}$$

The choice of the 0.15 as the upper limit in (3.4) allows at least 7–10 data points for tests with thin wave boundary layers. To account for the laminar sublayer and the buffer layer (Jiménez 2004), a lower data selection limit is imposed for flows over a smooth bottom:

$$z > 100\nu/u_{*m}. \tag{3.6}$$

It is found that PIV measurements are invalid for flows over rough bottoms in the region very close to the bottom roughness elements due to strong local laser reflection, so we also apply an alternative lower limit which requires that the percentage of good PIV measurements at a certain vertical level must exceed 75 %. This usually gives a lower limit between 0.5 and 1.5 mm above the top of bottom roughness elements. It should be noted that the spatial inhomogeneity of flow velocity due to individual bottom roughness elements is negligible at such a lower limit, i.e. the relative streamwise variation of the first-harmonic velocity amplitude is less than 5 %. The validity of these data selection limits is demonstrated by YM14. For fitting the upper current velocity profile, based on the improved GM model the lower limit for data selection is defined as

$$z > 1.5\delta_{ct}, \tag{3.7}$$

where δ_{ct} is the beginning of the upper logarithmic current profile according to the improved GM model. It is given by (A 2)–(A 7) using experimental values of A_{bm}/k_b and $\alpha = u_{*c}/u_{*m}$. Here u_{*c} and u_{*m} can be experimentally determined in advance by analysing the instantaneous bottom shear stress inferred from instantaneous velocity

	$1-R^2$	u_* (cm s^{-1})	$\pm\Delta u_*/u_*$ (%)	k_b (mm)	$r_{\Delta k}$
Current (lower part) $u_* = u_{*c,1}$	2.4×10^{-3}	3.3	5.0	18.6	1.14
Current (upper part) $u_* = u_{*c,2}$	5.3×10^{-4}	8.4	1.0	189.3	1.03
Wave $u_* = u_{*w,1}$	5.2×10^{-4}	17.9	2.3	19.4	1.06

TABLE 3. Log-profile fitting of the current velocity profile and the first-harmonic amplitude profile of Test SP400a_C40_ce ($1-R^2$: coefficient of determination; u_*: fitted shear velocity; $\pm\Delta u_*/u_*$: relative 95 % confidence interval of u_*; k_b: fitted bottom roughness; $r_{\Delta k}$: 95 % confidence factor of k_b).

profiles (see § 3.1.2). The safety factor of 1.5 in (3.7) is applied to account for the uncertainty in δ_{ct}. Since the current in the WCS is driven by a depth-invariant mean pressure gradient, τ_c should decay approximately linearly from the bottom to the edge of the bottom current boundary layer $z=\delta_c$, resulting in the following upper current velocity profile (with (3.1) for ν_t):

$$\bar{u} = \frac{u_{*c}}{\kappa}\ln\left(\frac{z}{z_{0a}}\right) - \frac{u_{*c}z}{\kappa\delta_c}. \tag{3.8}$$

For all tests in this study, the apparent roughness is in general between 1 and 20 cm, and current boundary layer thickness, δ_c, can be roughly estimated to be 250 mm, i.e. half of the test channel depth. With these representative values, we estimate that the second term in (3.8) is no more than 7–15 % of the first term below $z=100$ mm, indicating that the measured current velocity profile can be considered in agreement with the GM model's prediction. Thus, $z=100$ mm is applied as the upper limit for data selection when analysing current velocity profiles in the outer region.

The results of log-profile fittings for the representative test are shown in table 3. The quality of log-profile fitting is quantified by the coefficient of determination R^2 ($R^2=1$ indicating a perfect fit). The confidence level for u_* is given by a normalized 95 % confidence interval $\Delta u_*/u_*$, and the confidence level for k_b is indicated by a 95 % confidence factor $r_{\Delta k}\geqslant 1$, i.e. the true k_b is 95 % likely to fall between $k_b/r_{\Delta k}$ and $k_b\, r_{\Delta k}$. The lower current velocity profile has only 8 data points for log-profile fitting, so it gives the largest value of $1-R^2$ (of the order of $O(10^{-3})$), and consequently the largest $\Delta u_*/u_*$ (5 %) and $r_{\Delta k}$ (1.14). These confidence intervals are small enough to be considered acceptable. For collinear wave–current flows, the maximum combined bottom shear stress τ_{bm} is the sum of current bottom shear stress τ_{cb} and the maximum wave bottom shear stress τ_{wm}, so the following relationship between shear velocities is obtained:

$$u_{*c}^2 + u_{*wm}^2 = u_{*m}^2. \tag{3.9}$$

According to (3.2), (3.3) and (3.9), adding the shear velocity inferred from the lower current profile $u_{*c,1}=u_{*c}^2/u_{*m}=3.3$ cm s^{-1} and the shear velocity inferred from the first-harmonic velocity amplitude profile $u_{*w,1}=u_{*wm}^2/u_{*m}=17.9$ cm s^{-1} gives the maximum shear velocity $u_{*m}=3.3$ cm s^{-1} + 17.9 cm s^{-1} = 21.2 cm s^{-1}. Invoking $u_{*c,1}=u_{*c}^2/u_{*m}$, we therefore get $u_{*c}=\sqrt{u_{*c,1}\,u_{*m}}=\sqrt{3.3\times21.2}=8.4$ cm s^{-1}. This is identical to the shear velocity inferred from the upper current profile $u_{*c,2}=u_{*c}=8.4$ cm s^{-1}. As will be discussed in § 3.1.2, the experimental values of u_{*c} and u_{*m} can be directly determined from log-profile fitting instantaneous velocity profiles. For this test, the direct measurements of u_{*c} and u_{*m} are 8.8 cm s^{-1}

and 21.0 cm s^{-1}, respectively, which are in excellent agreement with the fitted values (8.4 and 21.2 cm s^{-1}). Therefore, the internal relationship among various shear velocities suggested by the GM model is validated by this representative test. Other sinusoidal-wave–current tests yield similar quantitative comparisons.

The first-harmonic velocity amplitude profile and the lower current velocity profile shown in figure 5(*a,b*) give values of k_b of 18.6 and 19.4 mm. These two values agree well with the predetermined Nikuradse equivalent sand grain roughness of the ceramic-marble bottom, $k_N = 20$ mm, so both the lower current velocity and the wave velocity profiles are controlled by the physical bottom roughness. In most theoretical models, the no-slip boundary condition is applied at $z = z_0 = k_b/30$ for both waves and currents. Our experimental results justify the validity of this choice. The upper current velocity profile in figure 5(*a*) gives an apparent roughness $k_a = 30z_{0a}$ of 189.3 mm which is an order of magnitude larger than the physical bottom roughness. The improved GM model gives the following formula for k_a:

$$\frac{k_a}{k_b} = \frac{1}{\alpha}\left(\frac{5\delta_w}{ek_b}\right)^{1-\alpha}, \tag{3.10}$$

where δ_w is a characteristic wave boundary layer thickness. Using measured k_b and α and applying (A 3)–(A 5) to give δ_w, (3.10) predicts $k_a = 213$ mm, which is in good agreement with the fitted value.

These analyses suggest that the GM model (with the improvements provided by Humbyrd 2012) has very good ability in predicting collinear sinusoidal waves and currents in OWTs.

3.1.2. *Bottom shear stress*

The instantaneous bottom shear stress is obtained by log-profile fitting the instantaneous Reynolds-averaged velocity profiles. This method assumes that in the very-near bottom region oscillatory boundary layer flows are quasi-steady, so instantaneous Reynolds-averaged velocity profiles are logarithmic and controlled by the physical bottom roughness k_b and the instantaneous shear velocities $u_*(t)$. The validity of this method is supported by Jensen *et al.* (1989) who directly measured the bottom shear stress for smooth oscillatory boundary layers using hot-film probes and found that their direct measurements were in good agreement with the estimates given by log-profile fittings. YM14 compared this method to other common methods for inferring bottom shear stress from velocity measurements, and demonstrated that this is the only valid method for rough-bottom tests in OWTs. To ensure that the selected data points correspond to near-bottom conditions, we simply use the bottom-most five data points which satisfy the previously stated data selection rules. A complete log-profile fitting analysis would take both k_b and $u_*(t)$ as unknowns to be determined, but most theoretical models, including the one presented in § 4, assume k_b as time-invariant. Therefore, here we adopt a modified log-profile fitting which has a predetermined k_b given by preliminary wave-alone and current-alone tests (see § 2.2), so that it is consistent to compare the experimental results with model predictions. However, it should be noted that the difference between the modified and the complete log-profile analyses can be up to 10–15 % for the maxima of bottom shear stress, which indicates the uncertainty in the experimental results and should be considered when interpreting potential differences between predicted and measured net sediment transport rates in the WCS.

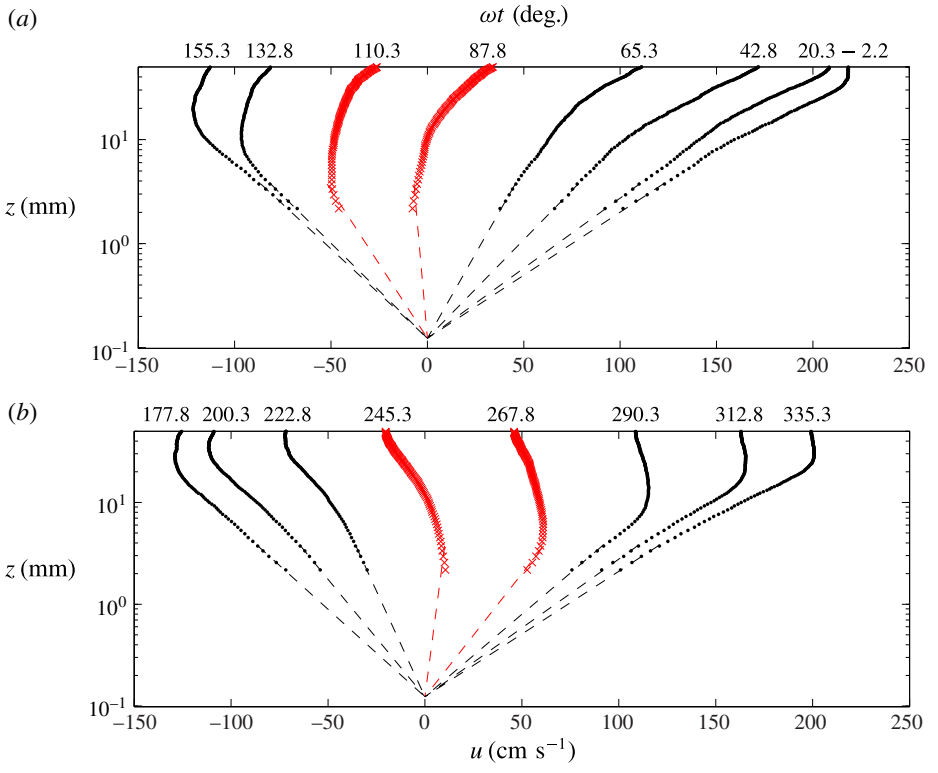

FIGURE 6. (Colour online) Instantaneous Reynolds-averaged velocity profiles of test SP400a_C40_sa and the associated modified log-profile fittings with $k_b = 3.7$ mm (grey crosses (red online): measurements with questionable log-profile fittings; dots: measurements with good log-profile fittings; dashed lines: fitted logarithmic profiles): (*a*) first half-period; (*b*) second half-period.

Figure 6 shows the instantaneous velocity profiles and the modified log-profile fittings for every $\Delta\omega t = 22.5°$ for a representative test, SP400a_C40_sa (the strongest sinusoidal waves plus the strongest current over the sandpaper bottom with $k_b = 3.7$ mm). For most velocity profiles, the fitted logarithmic profiles reasonably represent the bottom-most measurements, and the coefficient of determination R^2 is >0.99. For two short time windows when the free-stream velocity $u_\infty(t)$ crosses zero, i.e. the velocity profiles marked by crosses in figure 6, the fitted logarithmic profiles cannot reasonably approximate the measurements. As $u_\infty(t)$ decreases to zero, $\partial p/\partial x$ has the same sign as $u_\infty(t)$ and generally increases with ωt. Therefore, the instantaneous flow experiences an increasingly adverse pressure gradient, which eventually leads to flow separation, e.g. at $\omega t = 87.8°$ or 245.3°. The same feature is also observed for experiments over the smooth and ceramic-marble bottoms, as well as many previous turbulent wave-alone boundary layers, e.g. Jensen *et al.* (1989). Nevertheless, since $u_*(t)$ at these instants is close to zero, it is still acceptable to apply the modified log-profile fitting to the bottom-most five points and use the fitted $u_*(t)$, which is also close to zero, as a rough estimate of the actual value. This will at least give the correct direction of the instantaneous bottom shear stress, e.g. the fitted profile at $\omega t = 87.8°$ in figure 6 has a negative slope. The duration when the

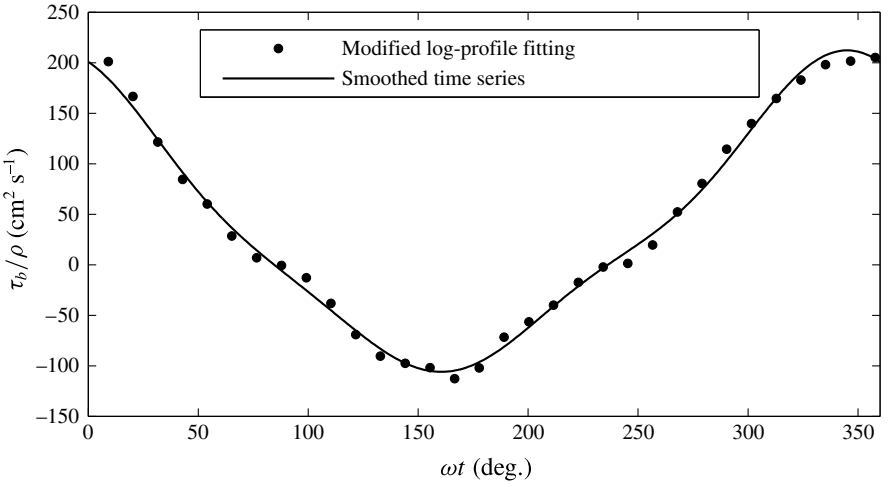

FIGURE 7. The bottom shear stress of test SP400a_C40_sa: modified log-profile fitting with bottom roughness $k_b = 3.7$ mm, and smoothed time series for modified log-profile fitting.

log-profile fitting is not good is roughly 20–30 % of the total wave period, so this method works well for most of a wave period.

Figure 7 shows the time series of bottom shear stress of test SP400a_C40_sa obtained from the modified log-profile fitting analysis, as well as a smoothed time series which only contains the mean and first three harmonics of the original time series. The smoothed time series nicely represents the data points, indicating that higher-order harmonics are negligibly small and have similar behaviour to experimental noise, but it does not represent the data points around zero-crossings very well, which is due to the effect of boundary layer separation. The current bottom shear stress τ_{cb} is obtained by period-averaging, and the maximum bottom shear stress τ_{bm} is obtained from the smoothed time series. The current bottom shear stress, τ_{cb}, is usually considered an input parameter for experiments and theoretical models, so we shall not discuss it here but use it for model validations in § 5. The difference between τ_{bm} and τ_{cb} is considered to be the maximum wave bottom shear stress, $\tau_{wm} = \tau_{bm} - \tau_{cb}$, which can be expressed by a wave friction factor f_{wc}:

$$f_{wc} = \frac{2\tau_{wm}}{\rho {U_{bm}}^2}. \tag{3.11}$$

The improved GM model developed by Humbyrd (2012) suggests that f_{wc} depends on the relative bottom roughness A_{bm}/k_b and the current condition represented by the parameter C_μ:

$$C_\mu = \tau_{bm}/\tau_{wm} = (1-\alpha^2)^{-1}. \tag{3.12}$$

By approximating the exact analytical solution, Humbyrd (2012) obtained a simple explicit expression for f_{wc} in the region $10 < X_\mu < 10^5$:

$$\frac{f_{wc}}{C_\mu} = \exp\left\{5.70(X_\mu)^{-0.101} - 7.46\right\}, \tag{3.13}$$

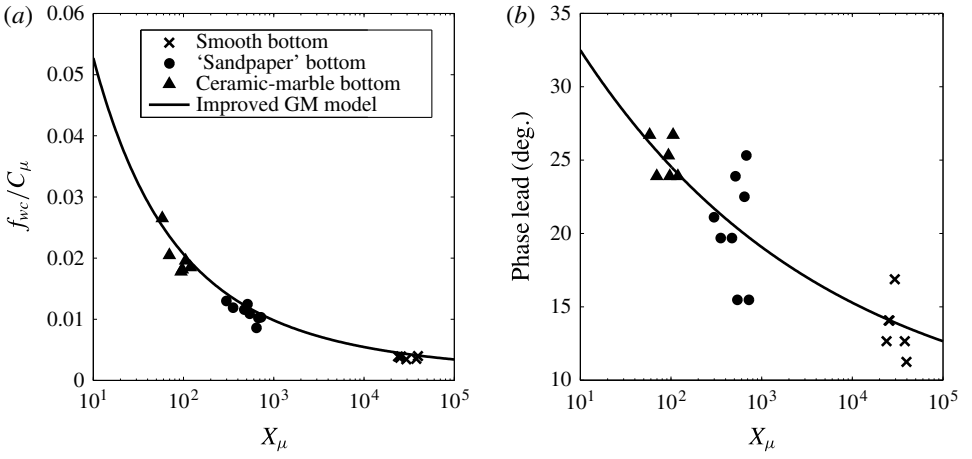

FIGURE 8. (*a*) Wave friction factors and (*b*) phase leads of the maximum wave bottom shear stress of combined sinusoidal-wave–current flows: smooth-bottom tests, sandpaper-bottom tests, ceramic-marble-bottom tests and the improved GM model).

where

$$X_\mu = C_\mu \frac{A_{bm}}{k_b}. \tag{3.14}$$

The maximum wave bottom shear stress τ_{wm} leads the free-stream velocity by a phase lead $\varphi_{\tau wm}$. For $10 < X_\mu < 10^5$, the improved GM model suggests that $\varphi_{\tau wm}$ can be approximately expressed as

$$\varphi_{\tau wm}\,(\text{deg.}) = (0.649 X_\mu^{-0.160} + 0.118)\, 180/\pi. \tag{3.15}$$

With $C_\mu = 1$, (3.13) and (3.15) give the friction factor and phase lead for turbulent sinusoidal-wave boundary layers. We can plot the measured variations of f_{wc}/C_μ and $\varphi_{\tau wm}$ against X_μ and compare this with the predictions of (3.13) and (3.15), as shown in figure 8. The measurements of f_{wc}/C_μ have little scatter and form a consistent decreasing trend with increasing X_μ. The improved GM model reasonably captures the observed trend, although it slightly overestimates the friction factors by roughly 10 %. Such a small error is insignificant compared to the potential uncertainty in the determination of the bottom roughness, so the model's performance can be considered excellent. This is not surprising, since the model's time-invariant turbulent eddy viscosity is scaled by the maximum shear velocity u_{*m}, which works ideally for predicting the maximum bottom shear stress. The measurements of $\varphi_{\tau wm}$ exhibit noticeable scatter, especially for the sandpaper-bottom tests (up to 5°). Nevertheless, the data points suggest that $\varphi_{\tau wm}$ decreases with increasing X_μ in a manner that is reasonably represented by the improved GM model, i.e. the data points appear to be distributed evenly on both sides of the curve. Given the fact that the amplitude is also well predicted, the performance of the improved GM model for prediction of the maximum wave bottom shear stress associated with combined collinear wave–current flows can be considered excellent.

3.2. *The effect of wave nonlinearity on wave–current interaction*

For pure nonlinear waves in OWTs, YM14 showed that a very weak mean velocity, the TA-streaming, is present. It is negative (opposing the wave direction) in the very

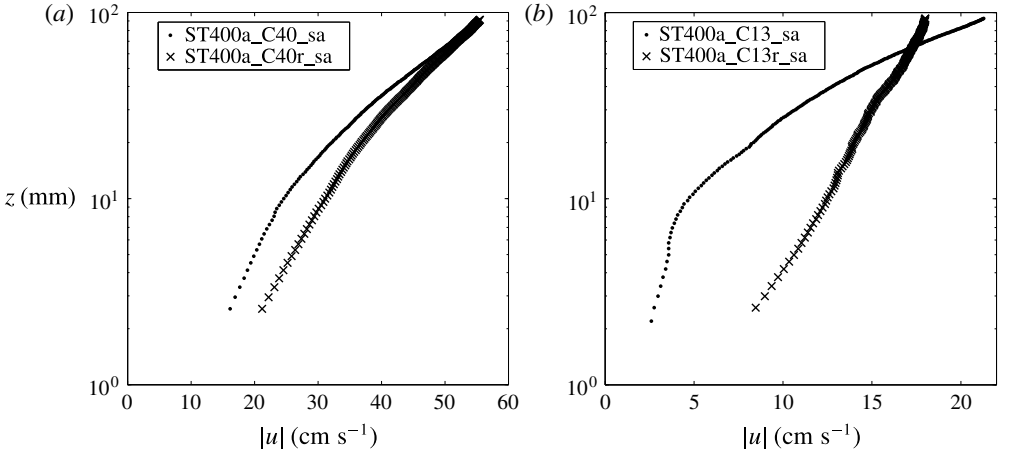

FIGURE 9. Magnitudes of measured current velocity profiles of the ST400a wave plus currents over the sandpaper bottom (dots: positive currents (in the wave direction); crosses: negative currents (against the wave direction): (*a*) strong (C40) currents; (*b*) weak (C13) currents.

near-bottom region, but becomes positive (following the wave direction) at higher elevations to balance the total volume flux. In this section, we briefly present some experimental results for nonlinear-wave–current flows in the WCS with focus on the current velocity profile, since the wave velocity is found to experience little influence from the superimposed current.

Unlike sinusoidal waves, nonlinear waves have direction dependence, so we consider collinear currents with different directions. Figure 9 shows measured current velocity profiles of four typical tests over the sandpaper bottom. They have the same wave conditions, i.e. the strongest Stokes waves ST400a (first-harmonic velocity amplitude of approximately 160 cm s^{-1} and 6.25 s wave period), but different current conditions. Figure 9(*a*) shows the current velocity profiles of the strong superimposed current C40 (roughly 46 cm s^{-1} cross-section average velocity) following or opposing the wave direction, while figure 9(*b*) shows the same comparison for the weak superimposed current C13 (roughly 15 cm s^{-1} cross-section average velocity). Here the magnitudes of measured current velocities are shown for easy comparison of currents in the two directions. The measurements suggest a pronounced difference between currents following or opposing nonlinear waves. In the very near-bottom region, the negative currents (shown by crosses) are stronger than the positive currents (shown by dots), but the discrepancy decreases with increasing elevation z. For the two strong-current tests, the two current velocity profiles do not intersect within the range of observation, but there is a clear indication of crossing at a higher level. The GM-type model's two-log-profile feature is observed for both of them, but is less pronounced for the negative current. For the weak-current tests, the two velocity profiles intersect at approximately $z = 65$ mm, and the positive current becomes increasingly stronger than the negative current above this level. The two-log-profile structure is completely obliterated for the negative current, while according to the GM model this feature should be very significant for weak currents plus strong waves, as demonstrated by the velocity profile of the positive C13 current.

The observed differences between currents following and opposing nonlinear waves agree qualitatively with the numerical results given by Holmedal *et al.* (2013),

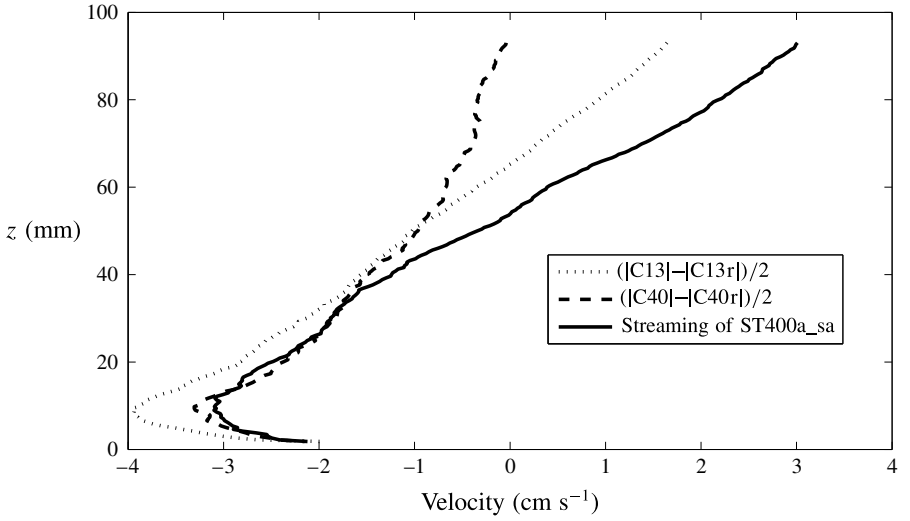

FIGURE 10. Estimate of the embedded mean velocity of test ST400a_sa (dotted line: based on C13 currents; dashed line: based on C40 current; solid line: measured mean velocity of test ST400a_sa).

and can be explained by TA-streaming produced by wave nonlinearity. The mean velocity profile embedded in the pure wave test ST400a_sa, which indicates the TA-streaming, is indicated by the solid line in figure 10. Such a mean velocity profile was first reported by Ribberink & Al-Salem (1995). Thus, if added to the two-log-profile structure suggested by the GM model, in the very near-bottom region this mean velocity will enhance a negative superimposed current but suppress a positive superimposed current, while the situation reverses at higher elevations. As a confirmation, we subtract the magnitude of the negative current profile from the magnitude of the positive current profile shown in figure 9(*a,b*) and divide the difference by 2. The obtained results shown in figure 10 agree well with the measured mean velocity embedded in test ST400a_sa, i.e. the three profiles are all negative in the very near-bottom region and reach minima of comparable magnitudes (-3 to -4 cm s^{-1}) at approximately the same level $z \approx 10$ mm, and the negative values decrease and eventually become positive at higher elevations.

The GM model is entirely blind to the direction of currents, since it is based on sinusoidal waves, and it will always give a two-log-profile structure of the current velocity profile, which is completely absent for the test with a weak negative current, ST400a_C13r_sa. Therefore, the GM model is incapable of modelling nonlinear-wave–current flows, especially for a wave with strong nonlinearity plus a weak current. If one were to blindly apply the GM model to analyse field measurements obtained in relatively shallow waters where the waves are nonlinear, the obtained results, e.g. current shear velocity u_{*c}, apparent roughness k_a or physical bottom roughness k_b, would be unreliable. In such situations, it is necessary to have a more elaborate wave–current boundary layer model which can consider the wave nonlinearity characterized by a second-harmonic free-stream velocity and a time-varying turbulent eddy viscosity.

4. Theoretical model

4.1. *Governing equations*

Oscillatory flows in OWTs are uniform in the longitudinal direction of the test channel, so the governing momentum equation is

$$\frac{\partial u}{\partial t} = -\frac{\partial (p/\rho)}{\partial x} + \frac{\partial (\tau_{zx}/\rho)}{\partial z}, \tag{4.1}$$

where u is the Reynolds-averaged velocity in the horizontal direction, x and z are the horizontal and vertical coordinates, t is time, ρ is fluid density, p is pressure and τ_{zx} is the component of the Reynolds stress which can be related to the Reynolds-averaged velocity through the concept of a turbulent eddy viscosity ν_t. The pressure gradient $\partial p/\partial x$ is considered depth-invariant, and its oscillatory part is related to the free-stream flow as

$$-\frac{1}{\rho}\frac{\partial \tilde{p}}{\partial x} = \frac{\partial \tilde{u}_\infty}{\partial t}, \tag{4.2}$$

where $\tilde{u}_\infty$ is the oscillatory part of the free-stream velocity. The time-invariant part of the pressure gradient can be neglected if we only consider the very near-bottom part of the current boundary layer. For the currents in the WCS, we have discussed that the mean pressure gradient will not invalidate the logarithmic profile and hence can be generally neglected in the region less than 100 mm from the bottom. For mathematical convenience, we define a velocity deficit:

$$u_d = u - \tilde{u}_\infty, \tag{4.3}$$

so (4.1) can be rewritten as

$$\frac{\partial u_d}{\partial t} = \frac{\partial}{\partial z}\left(\nu_t \frac{\partial u_d}{\partial z}\right). \tag{4.4}$$

It is customary to split u_d into a wave (time-dependent) velocity $\tilde{u}_d$ and a current (time-invariant) velocity $\bar{u}$ as

$$u_d = \tilde{u}_d + \bar{u} \tag{4.5}$$

where $\tilde{u}_d$ is expressed in the following general form:

$$\tilde{u}_d(z, t) = \mathrm{Re}\sum_{n=1}^{\infty} U_d^{(n)}(z)\mathrm{e}^{\mathrm{i}n\omega t}. \tag{4.6}$$

The wave velocity must converge to the free-stream value asymptotically and satisfy the no-slip boundary condition which is prescribed at $z = z_0 = k_b/30$. Therefore, the following boundary conditions are prescribed for the complex amplitude of nth-harmonic velocity deficit $U_d^{(n)}(z)$:

$$U_d^{(n)} = -U_\infty^{(n)}, \quad z = z_0, \tag{4.7}$$

$$U_d^{(n)} \to 0, \quad z \to \infty, \tag{4.8}$$

where $U_\infty^{(n)}$ is the complex amplitude of nth-harmonic free-stream velocity. For $\bar{u}$, the no-slip boundary condition also applies:

$$\bar{u} = 0, \quad z = z_0. \tag{4.9}$$

The other boundary condition is specified as a reference current velocity u_r at a reference elevation z_r:

$$\bar{u} = u_r, \quad z = z_r. \tag{4.10}$$

4.2. *Turbulent eddy viscosity*

For oscillatory turbulent boundary layers, Trowbridge & Madsen (1984*a*,*b*) suggested that the flow can be considered quasi-steady in the very near-bottom region, so the following expression for the turbulent eddy viscosity ν_t, obtained by generalizing the well-known results for steady turbulent boundary layer flows, is applicable in the immediate vicinity of the bottom:

$$\nu_t = \kappa \sqrt{\frac{|\tau_b(t)|}{\rho}} z = \kappa |u_*(t)| z. \tag{4.11}$$

Therefore, the temporal variation of ν_t is characterized by the temporal variation of $|u_*(t)|$, which can be expressed as

$$|u_*(t)| = \bar{u}_* f(t), \tag{4.12}$$

where $\bar{u}_*$ is the period average of $|u_*(t)|$ and $f(t)$ is a dimensionless temporal variation function which is always positive and has an period-averaged value of 1. Thus, (4.11) can be rewritten as

$$\nu_t = \bar{\nu}_t(z) f(t), \tag{4.13}$$

where $\bar{\nu}_t(z)$ is the time-averaged turbulent eddy viscosity. Although at higher elevations the temporal variation of ν_t may not be synchronized with that in the very near-bottom region, which means that $f(t)$ also varies with z, Trowbridge & Madsen (1984*a*,*b*) ignored this for mathematical convenience. Such a simplification will certainly deteriorate the prediction in the upper part of the boundary layer, but the flow in the very near-bottom region, which is critical for the determination of bottom shear stress, is still well-predicted. Therefore, in our theoretical model ν_t is treated as the product of a temporal variation function $f(t)$ and a mean turbulent eddy viscosity $\bar{\nu}_t(z)$ over the entire boundary layer.

We can always express $f(t)$ in terms of a Fourier series:

$$f(t) = 1 + a_1 \cos(\omega t + \psi_1) + a_2 \cos(2\omega t + \psi_2) + \cdots. \tag{4.14}$$

For sinusoidal waves, only the even harmonics of $f(t)$ exist since the two half-periods of $|u_*(t)|$ must be identical. For nonlinear waves, the two half-periods of $|u_*(t)|$ are asymmetric, e.g. the positive half-period of a Stokes wave will have larger maximum $|u_*(t)|$ than the negative half period, so odd harmonics of $f(t)$ are produced. The leading odd harmonic is the first harmonic $a_1 \cos(\omega t + \psi_1)$, which interacts with the first-harmonic velocity gradient to produce a non-zero period-averaged shear stress. This is the origin of the TA-streaming (Trowbridge & Madsen 1984*b*). It should be noted that a superimposed current can also give rise to odd harmonics of $f(t)$, so TA-streaming also exists for sinusoidal-wave–current boundary layer flows.

By only retaining the first and second harmonics of $f(t)$, Trowbridge & Madsen (1984*a*,*b*) used perturbation methods to analytically study sinusoidal turbulent wave boundary layers (first-order analysis) and weakly nonlinear progressive waves (second-order analysis), but external currents were not considered in their study. Following their work, Gonzalez-Rodriguez & Madsen (2011) studied nonlinear waves and wave–current flows in OWTs. Their predictions of TA-streaming for Stokes waves were in good agreement with measurements, but their predictions for forward-leaning waves and wave–current flows were not very successful. This is because they assumed that

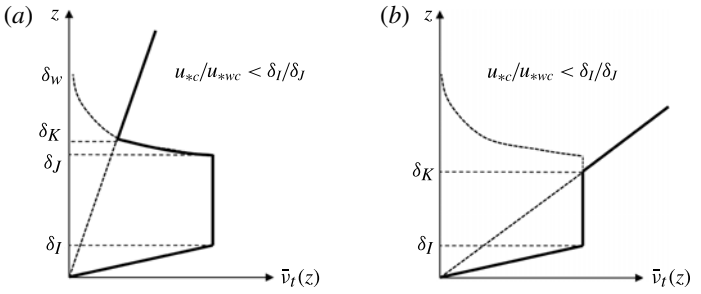

FIGURE 11. Vertical structure of the time-averaged turbulent eddy viscosity for oscillatory turbulent boundary layer flows: (*a*) weak current; (*b*) strong current.

the first and second harmonics of $f(t)$ are very small, i.e. $a_1, a_2 \ll 1$ in (4.14), which is necessary for the neglect of higher-order terms. However, the predicted values of a_1 and a_2 contradict this assumption, e.g. the value of a_2 is around 0.4 which is hardly a very small number. Therefore, in § 4.3 we will develop a semi-analytical approach which does not make prior assumptions on the magnitudes of certain parameters.

The three-layer turbulent eddy viscosity of the improved GM model, i.e. (A 1), may be questionable for very weak currents, i.e. for very small α, the δ_{ct} given by (A 7) will be larger than δ_w, meaning that the wave-produced turbulence still controls the current even far outside the wave boundary layer, in violation of the basic assumption of the GM model. To remove this inconsistency, we propose the following four-layer vertical structure for $\bar{\nu}_t(z)$:

$$\bar{\nu}_t(z) = \begin{cases} \kappa \bar{u}_* z, & z_0 \leqslant z < \delta_I, \\ \kappa \bar{u}_* \delta_I, & \delta_I \leqslant z < \delta_J, \\ \kappa \bar{u}_* \delta_I \exp\left\{-\gamma \dfrac{z-\delta_J}{\kappa \bar{u}_*/\omega}\right\}, & \delta_J \leqslant z < \delta_K, \\ \kappa u_{*c} z, & \delta_K \leqslant z. \end{cases} \tag{4.15}$$

A graphical representation of this vertical structure is shown in figure 11. Without the top-most current-dominated layer, the first three layers collectively give the $\bar{\nu}_t(z)$ of a pure wave boundary layer, which approximates a parabolic vertical structure scaled by the wave boundary layer thickness δ_w:

$$\bar{\nu}_t(z) = \kappa \bar{u}_* z \left(1 - \frac{z}{\delta_w}\right), \quad z_0 \leqslant z \leqslant \delta_w. \tag{4.16}$$

Here δ_w is defined as the level where the amplitude of the first-harmonic velocity deficit reaches 1 % of the amplitude of the free-stream first-harmonic velocity. The choice of a parabolic structure as the target structure of the approximation is because this structure is commonly used for modelling steady open-channel turbulent flows. The transition levels (δ_I and δ_J) and the parameter γ are determined by requiring that the total area under the parabolic curve is maintained, which gives

$$\delta_I = 0.21\delta_w, \quad \delta_J = 0.79\delta_w, \quad \gamma = 9.5\frac{\kappa \bar{u}_*/\omega}{\delta_w}. \tag{4.17a–c}$$

The third layer makes the wave-produced $\bar{\nu}_t(z)$ decay exponentially with elevation, so the singularity $\bar{\nu}_t(\delta_w) = 0$ of the parabolic structure is avoided. The level δ_K is where

$\kappa u_{*c} z$ intersects the underlying three-layer structure. With the exponential-decaying layer, δ_K will be generally less than δ_w for most current conditions, e.g. figure 11(*a*), so the possible inconsistency of the improved GM model is avoided. When the superimposed current is sufficiently strong, i.e. $u_{*c}/\bar{u}_* > \delta_I/\delta_J = 0.27$, the intersection will be within the second layer, as shown in figure 11(*b*), so the exponential-decaying layer does not appear and the three-layer structure of the improved GM model is reproduced.

4.3. *A semi-analytical approach*

In this subsection, a semi-analytical approach for solving the governing equation introduced in § 4.1 with the turbulent eddy viscosity introduced in § 4.2 is briefly presented. With (4.13) and (4.5), (4.4) can be written as

$$\frac{\partial \tilde{u}_d}{\partial t} = \frac{\partial}{\partial z}\left(\bar{\nu}_t(z) f(t) \frac{\partial \tilde{u}_d}{\partial z}\right) + \frac{\partial}{\partial z}\left(\bar{\nu}_t(z) f(t) \frac{\partial \bar{u}}{\partial z}\right). \tag{4.18}$$

Instead of using the perturbation method as Gonzalez-Rodriguez & Madsen (2011), we divide all terms by $f(t)$ to get

$$\frac{\partial \tilde{u}_d}{f(t)\partial t} = \frac{\partial}{\partial z}\left(\bar{\nu}_t(z) \frac{\partial \tilde{u}_d}{\partial z}\right) + \frac{\partial}{\partial z}\left(\bar{\nu}_t(z) \frac{\partial \bar{u}}{\partial z}\right). \tag{4.19}$$

Following Lavelle & Mofjeld (1983), we define a new time variable:

$$\tau = \int f(t)\mathrm{d}t = t + h(t), \tag{4.20}$$

where, with $f(t)$ given by (4.14):

$$h(t) = \sum_{n=1}^{\infty} \frac{a_n}{n\omega} \sin(n\omega t + \psi_n). \tag{4.21}$$

We change the temporal variable of (4.19) to give

$$\frac{\partial \tilde{u}_d}{\partial \tau} = \frac{\partial}{\partial z}\left(\bar{\nu}_t(z) \frac{\partial \tilde{u}_d}{\partial z}\right) + \frac{\partial}{\partial z}\left(\bar{\nu}_t(z) \frac{\partial \bar{u}}{\partial z}\right). \tag{4.22}$$

This is the governing equation with a new temporal variable τ. For clarity, we denote the solution in τ-space by $V(z, \tau)$, and split (4.22) into a wave equation:

$$\frac{\partial \tilde{V}}{\partial \tau} = \frac{\partial}{\partial z}\left(\bar{\nu}_t(z) \frac{\partial \tilde{V}}{\partial z}\right) \tag{4.23}$$

and a current equation:

$$\frac{\partial}{\partial z}\left(\bar{\nu}_t(z) \frac{\partial \bar{V}}{\partial z}\right) = 0. \tag{4.24}$$

The oscillatory velocity in τ-space can be expressed in terms of a Fourier series:

$$\tilde{V}(z, \tau) = \mathrm{Re}\left\{\sum_{n=1}^{\infty} V^{(n)}(z) \mathrm{e}^{\mathrm{i}n\omega\tau}\right\}, \tag{4.25}$$

where $V^{(n)}$ is the complex amplitude of nth-harmonic velocity in τ-space:

$$V^{(n)}(z) = V_n(z)\exp(\mathrm{i}\varphi_{vn}(z)), \tag{4.26}$$

with $V_n(z)$ and $\varphi_{vn}(z)$ being the amplitude and phase of $V^{(n)}$, respectively. The wave equation is solved harmonic by harmonic:

$$\mathrm{i}n\omega V^{(n)} = \frac{\partial}{\partial z}\left(\bar{\nu}_t(z)\frac{\partial V^{(n)}}{\partial z}\right), \tag{4.27}$$

and, with $\bar{\nu}_t$ given by (4.15), both (4.24) and (4.27) are ordinary differential equations that can be solved analytically. The general analytical solutions obtained are converted back to t-space using (4.20), and the conversion requires some simple numerical Fourier analyses of given time series. It should be highlighted that a mean velocity, $\bar{u}_V(z)$, is produced when converting the wave solution from τ-space to t-space, which essentially represents the origin of the TA-streaming. Matching boundary conditions in t-space produces a set of linear equations for the unknown constants in the general solution. The reader is referred to Yuan (2013) for further details on approximately solving the wave equation using change of temporal variables.

The current equation is analytically solved as introduced in appendix B. The solution suggests that the total current velocity profile is the sum of the TA-streaming $\bar{u}_s$ (related to $\bar{u}_V(z)$), i.e. (B 5), and another mean velocity $\bar{u}_c$ given by solving the current equation in τ-space, i.e. (B 8). The latter is named the 'basic current' hereafter, because it is shown that the current bottom shear stress is solely produced by this basic current, while waves in OWTs will not create a mean bottom shear stress, regardless of the wave shape (see appendix B for details).

Since the solution requires ν_t which contains parameters given by model predictions, an iterative solution procedure is developed as follows. With the free-stream oscillatory velocity, the bottom roughness and the current reference velocity at $z = 100$ mm obtained from the measurements, we first apply the improved GM model (appendix A) to predict the current bottom shear stress τ_{cb} and the maximum wave bottom shear stress τ_{wm}, which together give a time series of the bottom shear stress as

$$\tau_b(t) = \tau_{wm}\cos(\omega t + \varphi_{\tau wm}) + \tau_{cb}. \tag{4.28}$$

We then analyse this time series to give initial values for $\{a_n\}$, $\{\psi_n\}$ and $\bar{u}_*$, which define the mean turbulent eddy viscosity $\bar{\nu}_t$ given by (4.15) and the temporal variation function $f(t)$ given by (4.14). The initial value of the boundary layer thickness δ_w is also given by the improved GM model. For simulating all tests in this study, this initiation never results in a divergence of the model results, and the solution converges quickly.

The governing equations are then solved as introduced above, so the remaining task is to obtain new estimates of the iterative parameters through a closure hypothesis. According to (4.12), we have

$$\bar{u}_* f(t) = \sqrt{\frac{|\tau_b(t)|}{\rho}} = \sqrt{\left|\kappa\bar{u}_* z_0 f(t)\frac{\partial u}{\partial z}\bigg|_{z=z_0}\right|}. \tag{4.29}$$

Since $\bar{u}_*$ and $f(t)$ are always positive by definition, this equation can be rewritten as

$$\bar{u}_* f(t) = \kappa z_0\left|\frac{\partial u}{\partial z}\bigg|_{z=z_0}\right|. \tag{4.30}$$

The right-hand side can be easily calculated from the solution for u, so the time series of $\bar{u}_* f(t)$ over a wave period is obtained. We numerically Fourier analyse it to give the mean and the Fourier components which define the values of $\bar{u}_*$, $\{a_n\}$ and $\{\psi_n\}$. In addition, the wave boundary layer thickness δ_w can also be determined using the solution of the first-harmonic velocity in t-space. These new values will replace the previous estimates and the procedure is repeated until the following convergence criteria are met:

$$\left|\frac{x_{new} - x_{old}}{x_{old}}\right| < 1\,\%, \quad x \sim \delta_w,\, u_{*c},\, \bar{u}_*,\, a_n \mathrm{e}^{\mathrm{i}\psi_n}. \tag{4.31}$$

Most of the iterative algorithms are expressed using matrices and vectors (see Yuan 2013 for details), so the solution procedure can be easily programmed in a manner that allows us to consider any number of terms of $\{a_n\}$, $\{\psi_n\}$ and $\{U^{(n)}\}$ by simply changing the sizes of these matrices and vectors. This is the advantage of this theoretical model over the analytical model of Gonzalez-Rodriguez & Madsen (2011), because we do not need to make prior assumptions on flow conditions to neglect higher-order terms, but simply keep adding terms until the predictions for the leading Fourier components of velocity and bottom shear stress converge. Thus, we essentially let the model tell us which higher-order terms can be neglected. For modelling the experimental results in this study, calculations show that it is only necessary to consider up to the fourth harmonic of ν_t and the fifth harmonic of velocity, since adding more harmonics will cause only minor changes to the quantities of primary interest, e.g. for Stokes waves over the range $10 < A_{bm}/k_b < 10^5$ the first three harmonics of bottom shear stress are changed by less than 0.5 %, 1.5 % and 5.0 % in amplitude, and less than 0.1°, 0.3° and 5.5° in phase, respectively, by adding higher-order harmonics.

5. Model validation

In this section, we validate the theoretical model for oscillatory turbulent boundary layer flows developed in § 4 against the experimental results shown in § 3.

5.1. *Wave velocity and wave bottom shear stress*

For simplicity, the validation of our theoretical model for pure wave boundary layer flows are presented based on three representative tests, SP400a_sa, ST400a_sa, and FL320_sa, corresponding to sinusoidal, Stokes and forward-leaning waves, respectively. These tests are all over the sandpaper bottom and have wave periods of 6.25 s. Their first-harmonic free-stream velocity amplitudes are the highest among tests with the same wave shape, i.e. the values of $U_{\infty,1}$ are roughly 160 cm s^{-1}, 160 cm s^{-1} and 126 cm s^{-1} for SP400a_sa, ST400a_sa, and FL320_sa, respectively. For sinusoidal wave boundary layers, the top-most current-dominated layer of the four-layer mean turbulent eddy viscosity is not considered since no current shear stress exists, and the model's algorithm is accordingly simplified. Because the two half-wave-periods of a sinusoidal wave are symmetric, the even-order harmonics of the velocity vanish, and therefore the following comparisons are based on the first- and third-harmonic velocities, as shown in figure 12. The model successfully predicts the first-harmonic velocity for sinusoidal waves in the immediate vicinity of the bottom (figure 12*a,b*), i.e. the logarithmic amplitude profile is predicted with a relative error less than 2 % below $z = 6$ mm, and the disagreement for the first-harmonic phase is within 1°–5°.

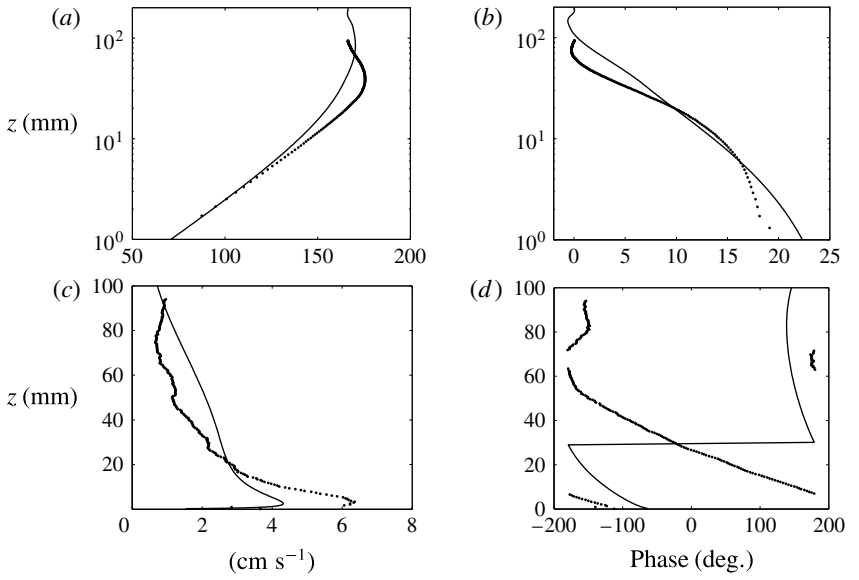

FIGURE 12. Prediction of the first- and third-harmonic velocities of sinusoidal wave test SP400a_sa (solid lines: predictions; dots: measurements): (*a*) first-harmonic amplitude, $|u^{(1)}(z)|$; (*b*) first-harmonic phase, $\mathrm{Arg}(u^{(1)}(z))$; (*c*) third-harmonic amplitude, $|u^{(3)}(z)|$; (*d*) third-harmonic phase, $\mathrm{Arg}(u^{(3)}(z))$.

The model's performance at higher elevations, however, is not as good as in the very near-bottom region, i.e. both the magnitudes and the locations of amplitude overshoots are not predicted very accurately. This is most likely due to oversimplification of the mean turbulent eddy viscosity $\bar{\nu}_t$, i.e. (4.15), in the upper part of wave boundary layer. Nevertheless, it is the very near-bottom region that plays a crucial role in determining bottom shear stress and sediment transport, so our model's prediction of the first-harmonic velocity of sinusoidal waves is still considered good. The third-harmonic velocity embedded in sinusoidal waves, as shown in figure 12(*c,d*), is a result of the temporal variation of turbulent eddy viscosity. The model to some extent predicts the overshoot structure of the third-harmonic velocity amplitude in the very near-bottom region, but the magnitudes are significantly underestimated. The third-harmonic phases are overpredicted in the very near-bottom region by 30°–50°, and the predictions in the upper part of the water column deviate even more significantly from the measurements. Therefore, it should be concluded that the model only qualitatively predicts the third-harmonic velocity. Nevertheless, the third-harmonic velocity is a very small component of the entire oscillatory velocity (3–5 %), and its contribution to bottom shear stress is negligible, so there is no necessity to predict it very accurately.

For Stokes and forward-leaning waves, the predictions of the first- and third-harmonic velocities lead to the same conclusions as for sinusoidal waves. The prediction of the mean velocity will be specifically discussed in the § 5.2, so here we will only discuss the predictions for second-harmonic velocities, as shown in figure 13. Generally speaking, the model's performance is very similar to that for the first-harmonic velocity of sinusoidal waves. For the Stokes-wave test (figure 13*a,b*), the near-bottom logarithmic amplitude profile is excellently predicted,

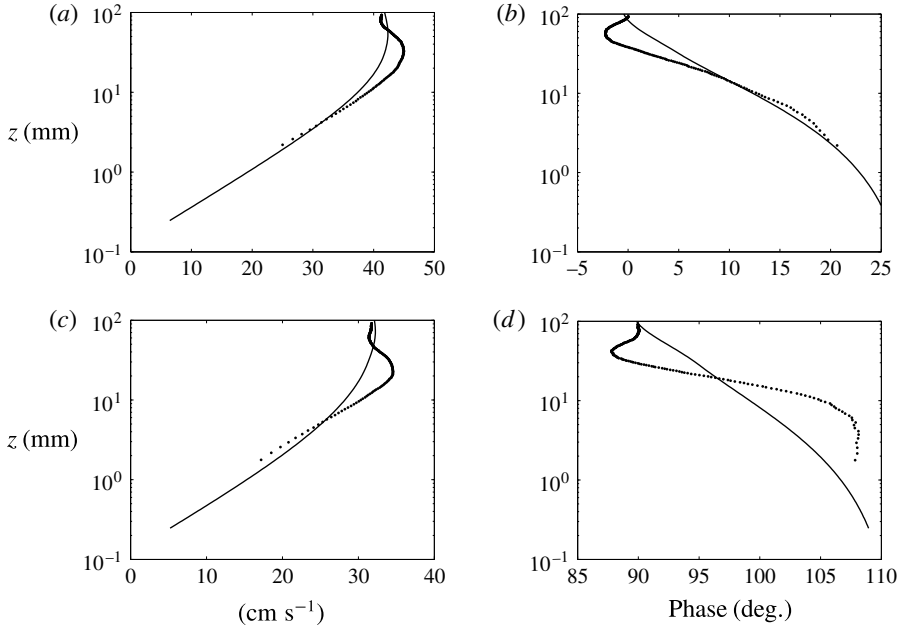

FIGURE 13. Prediction of the second-harmonic velocity of test ST400a_sa (Stokes waves) and FL320a_sa (forward-leaning waves) (solid lines: predictions; dots: measurements): (*a*) amplitude of test ST400a_sa, $|U^{(2)}(z)|$; (*b*) phase of test ST400a_sa, $\mathrm{Arg}(U^{(2)}(z))$; (*c*) amplitude of test FL320_sa, $|U^{(2)}(z)|$; (*d*) phase of test FL320_sa, $\mathrm{Arg}(U^{(2)}(z))$.

and second-harmonic phase is also reasonably predicted with an error less than 2°, but in the upper part of the boundary layer the agreement between measurements and predictions deteriorates, i.e. the vertical elevation of the maximum amplitude overshoot is still overestimated. For the forward-leaning-wave test (figure 13*c,d*), the prediction is not as good as for the Stokes-wave test. The prediction of the second-harmonic amplitude is no longer excellent in the very near-bottom region, i.e. the model overpredicts the amplitude by roughly 5 % below $z = 3$ mm, and the prediction of the second-harmonic phase is also worse, i.e. the measurements are nearly depth-invariant in the region a few millimetres above the bottom, but the predictions do not pick up this feature. Given that the second-harmonic velocity is only approximately 25 % of the first-harmonic velocity in magnitude, such an inaccuracy is still acceptable.

Although the overall performance of the theoretical model for predicting wave velocity is not excellent, it still accurately predicts the dominant harmonics of wave velocity in the very near-bottom region, which is essential for predicting wave bottom shear stress. The predicted time series of bottom shear stress for the three representative tests are compared with measurements obtained from modified log-profile fittings in figure 14. For all tests, the model predicts the positive and negative maxima of the bottom shear stresses with an accuracy better than 10 %. The temporal variation is also well predicted, e.g. the model accurately captures the asymmetry between the two wave half-periods for the two nonlinear-wave tests. Thus, the model can accurately predict bottom shear stress in the WCS, which is critical for future studies on fluid–sediment interaction.

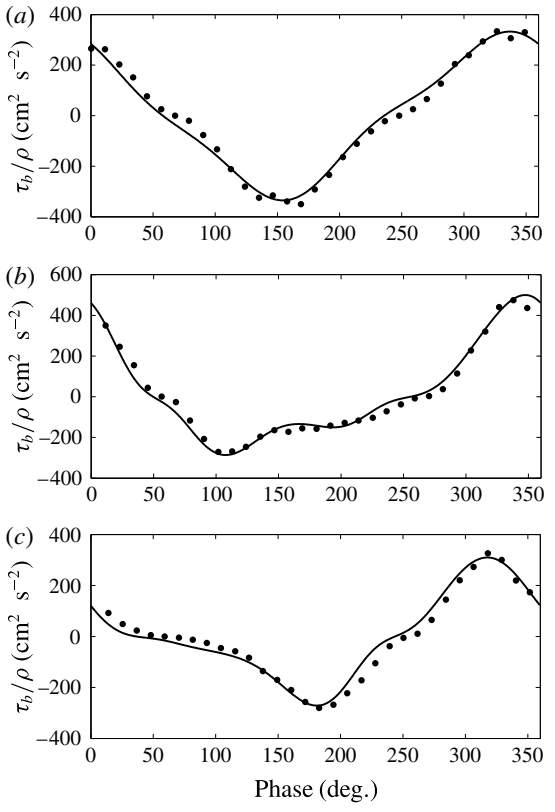

FIGURE 14. Prediction of wave bottom shear stress (solid lines: predictions; dots: measurements from modified log-profile fitting analysis with $k_b = 3.7$ mm): (*a*) test SP400a_sa (sinusoidal wave); (*b*) test ST400a_sa (Stokes wave); (*c*) test FL320_sa (forward-leaning wave).

5.2. *Mean velocity embedded in pure nonlinear-wave tests*

For six representative nonlinear-wave tests, the predictions of $\bar{u}$ are compared with measurements in figure 15. For the two ceramic-marble-bottom tests (figure 15*a,b*), the model accurately predicts the mean velocity in the very-near bottom region, i.e. the maximum negative velocity and the thickness of the negative-velocity region are both reasonably predicted. Above $z = 100$ mm, the location where the reference value of $\bar{u}$ is specified as a boundary condition, the neglected effect of the mean pressure gradient becomes significant, and the prediction deviates from measurements above $z = 100$ mm for some tests. The model prediction is also good for the two sandpaper tests (figure 15*c,d*). For the two smooth-bottom tests (figure 15*e,f*) the prediction is only qualitative, i.e. the overshoot is significantly overestimated (by a factor over 2). This is possibly because the viscous effect is not completely negligible as evidenced by the thickness of buffer layer estimated from (3.6) to be up to 2 mm. Therefore, it is concluded that the model can quantitatively predict the mean velocity embedded in nonlinear waves over rough bottoms, but its performance for smooth-bottom scenarios is only qualitatively acceptable.

The total mean velocity $\bar{u}$ embedded in a nonlinear wave in OWTs is the sum of a TA-streaming, $\bar{u}_s$, and a return current, $\bar{u}_c$. The present model can separately predict

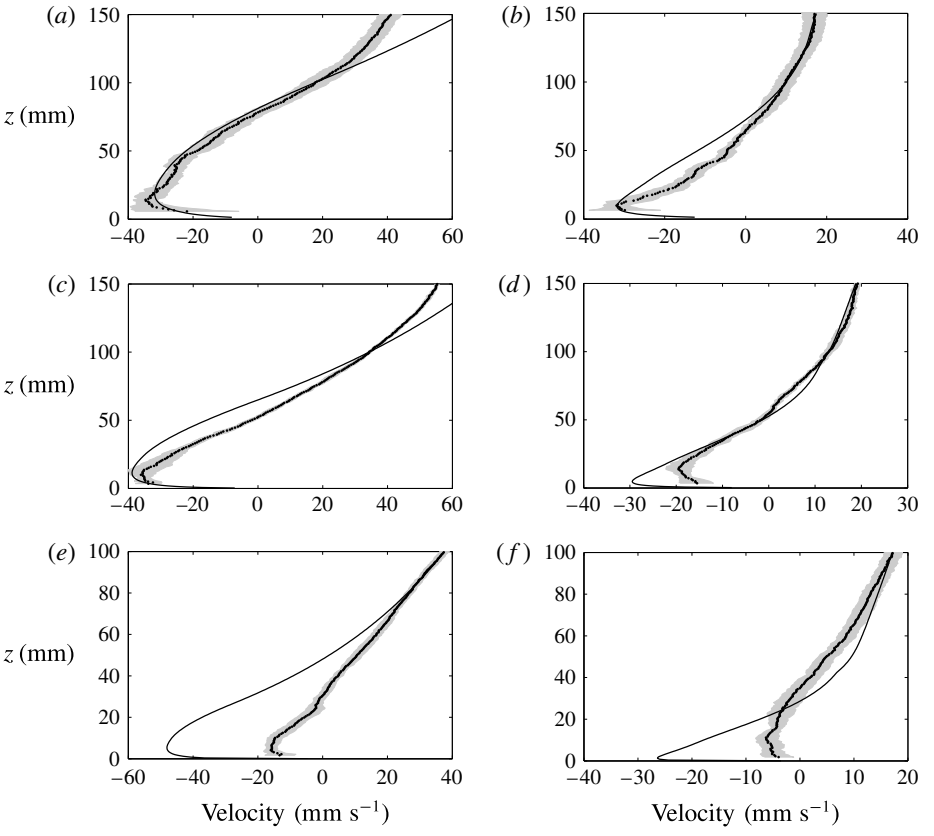

FIGURE 15. Prediction of the boundary layer streaming of the nonlinear waves (black dots: measurements; grey zones: standard deviations given by spatial averaging; solid lines: prediction): (*a*) ST400a_ce; (*b*) FL320a_ce; (*c*) ST400a_sa; (*d*), FL320a_sa; (*e*) ST400a_sm; (*f*) FL320a_sm.

$\bar{u}_s$ and $\bar{u}_c$, so it is of interest to investigate them individually. For simplicity, the following discussion is based on the two ceramic-marble-bottom tests ST400a_ce and FL320a_ce. In figure 16, the predicted total mean velocities $\bar{u}$ shown in figure 15(*a*,*b*) are decomposed into $\bar{u}_s$ and $\bar{u}_c$. For the nonlinear waves in this study, model predictions suggest that $\bar{u}_s$ can be approximately written as

$$\bar{u}_s(z) \approx \bar{u}_{s,1}(z) + \bar{u}_{s,2}(z), \tag{5.1}$$

where $\bar{u}_{s,n}$ can be approximated by (see Yuan 2013 for details)

$$\bar{u}_{s,n}(z) \approx \mathrm{Re}\left\{-\tfrac{1}{2}a_n \mathrm{e}^{-\mathrm{i}\psi_n} u^{(n)}(z)\right\}, \quad n = 1, 2. \tag{5.2}$$

It can be readily seen that $\bar{u}_{s,1}$ and $\bar{u}_{s,2}$ represent the TA-streaming produced by the first- and second-harmonic interactions of the time-varying velocity gradient and the time-varying turbulent eddy viscosity, since a_n represents the relative magnitude of the nth-harmonic turbulent eddy viscosity and $u^{(n)}(z)$ is the complex amplitude of the nth-harmonic velocity.

For the Stokes wave shown in figure 16(*a*), $\bar{u}_{s,1}$ and $\bar{u}_{s,2}$ are both negative over the entire boundary layer; $\bar{u}_{s,1}$ reaches -19.3 cm s^{-1} at $z = 100$ mm and is much

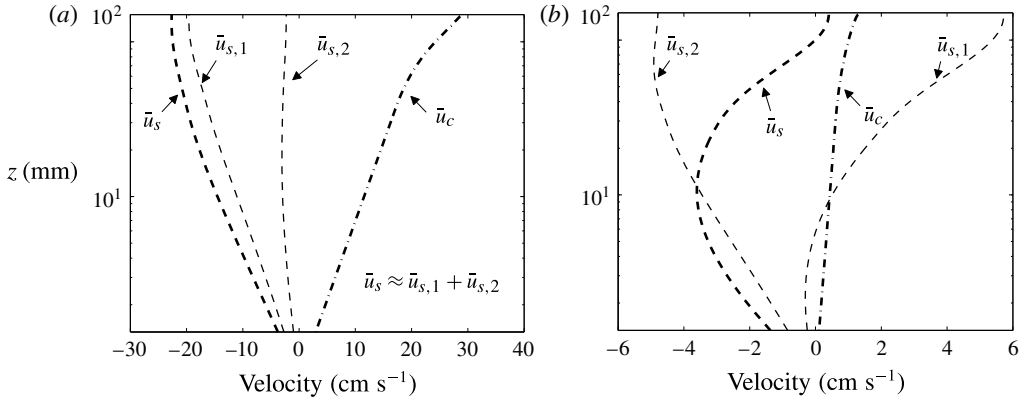

FIGURE 16. Decomposing of the mean velocity profile embedded in nonlinear waves (thick dashed lines: turbulence asymmetry streaming; thin dashed lines: main components of turbulence asymmetry streaming; thick dash-dot lines: basic (return) current): (*a*) Stokes wave (ST400a_ce); (*b*) forward-leaning wave (FL320a_ce).

stronger than $\bar{u}_{s,2}$ which is only -2.3 cm s^{-1} at the same level. Therefore, the total $\bar{u}_s$ is -22.5 cm s^{-1} at $z = 100$ mm, which is much stronger than the total mean velocity ($\bar{u} = 1.7$ cm s^{-1}) at $z = 100$ mm (see figure 15*a*). Thus, the superimposed return current $\bar{u}_c$ must be positive and have a magnitude comparable to $\bar{u}_s$, i.e. $\bar{u}_c$ is 24.2 cm s^{-1} at $z = 100$ mm. The predicted current shear velocity u_{*c} which controls $\bar{u}_c$ is 4.64 cm s^{-1}, and is in excellent agreement with the measurement $u_{*c} = 4.67$ cm s^{-1} obtained from log-profile fittings of the instantaneous velocity profiles (§ 3.1.2). Therefore, the observed mean velocity embedded in a Stokes wave is essentially a small imbalance between a sizeable TA-streaming and a sizeable return current. The reason for having such a strong $\bar{u}_{s,1}$ is that the first-harmonic turbulent eddy viscosity and the first-harmonic free-stream velocity are roughly in phase. For this test the predicted a_1 and ψ_1 are 0.28 and $-22°$, respectively, and the amplitude of $U_\infty^{(1)}$ is roughly 160 cm s^{-1}, so the asymptotic value of $\bar{u}_{s,1}$, according to (5.2), is approximately -20 cm s^{-1}, which is in agreement with the actual prediction (-19.3 cm s^{-1}).

The TA-streaming of forward-leaning waves is dramatically different from that of Stokes waves. As shown in figure 16(*b*), $\bar{u}_{s,1}$ is mostly positive over the entire boundary layer and its magnitude is slightly smaller than that of $\bar{u}_{s,2}$ which is always negative. Thus, the magnitude of $\bar{u}_s$ is quite small, and consequently the return current required to balance the total volume flux is weak, i.e. $\bar{u}_c$ is only 1.02 cm s^{-1} at $z = 100$ mm and the predicted u_{*c} is only 0.95 cm s^{-1} (the measured value is 1.36 cm s^{-1}). The reason for such a small and positive $\bar{u}_{s,1}$ for the forward-leaning wave is that the first-harmonic turbulent eddy viscosity is almost 90° out of phase with the first-harmonic velocity. The predicted ψ_1 is $-96°$, while the predicted a_1 is still 0.28. Thus, the absolute value of the complex number given by the right-hand side of (5.2) is still large (18 cm s^{-1}), but its real part is only 2 cm s^{-1}. Gonzalez-Rodriguez & Madsen (2011) only considered the first-harmonic interaction $\bar{u}_{s,1}$, which is the dominant one for Stokes waves but not for forward-leaning waves. Therefore, their model works for Stokes waves, but since $\bar{u}_{s,1}$ is dramatically different from the total $\bar{u}_s$, their prediction fails for forward-leaning waves. This suggests that the TA-streaming is very sensitive to the actual flow condition.

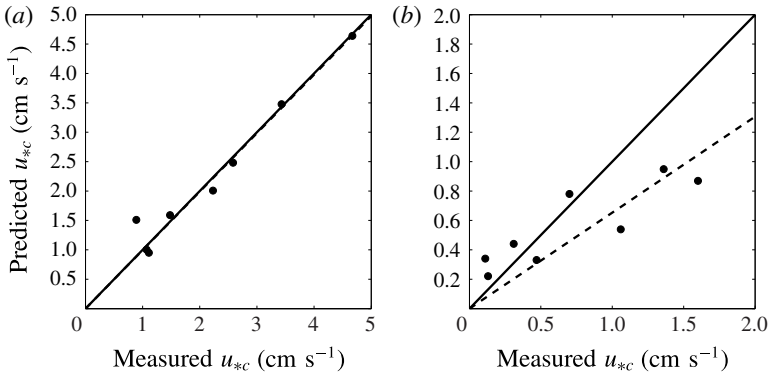

FIGURE 17. Comparison of the predicted and measured current shear velocity for nonlinear waves (solid line: perfect agreement; dashed lines: least-square fit to the data): (*a*) Stokes waves; (*b*) forward-leaning waves.

The predicted and measured mean bottom shear stresses are compared in terms of the current shear velocity u_{*c} in figure 17. For the Stokes-wave tests (figure 17*a*), the predictions on average deviate from the measurements by a mere 0.5 %. For the forward-leaning-wave tests, the agreement is still reasonable but not as good as for the Stokes-wave tests, i.e. the fitted dashed line in figure 17(*b*) corresponds to a slope of 0.65, indicating that the model underestimates u_{*c} by 35 %. This is partly because the forward-leaning-wave tests have much smaller u_{*c} than the Stokes-wave tests, so the same absolute experimental and model inaccuracies will result in a larger relative error. At the same time, the model's performance in predicting the mean velocity is generally worse for forward-leaning waves, as shown in figure 15, consequently the model's inaccuracy in predicting the mean bottom shear stress for forward-leaning waves is expected to be larger.

The analytical solution for the mean velocity indicates that the mean bottom shear stress is solely related to the return current, so it will not be the same if the waves are produced in real coastal waters, and hence has little value for practical applications. However, this mean bottom shear stress is very important for interpreting measurements of net sediment transport under pure nonlinear waves in OWTs, such as the experimental results reported by Ribberink & Al-Salem (1995), O'Donoghue & Wright (2004), van der A, O'Donoghue & Ribberink (2010) and Ruessink *et al.* (2011). Generally speaking, the wave nonlinearities make the maximum onshore (positive) bottom shear stress τ_{bm+} stronger than the maximum offshore (negative) bottom shear stress τ_{bm-}, so a net onshore sediment transport, which is closely related to the difference between the two maxima, is produced. When studying this phenomenon using OWTs, the additional positive mean bottom shear stress produced by the return current will enhance this difference, and therefore increase the net onshore sediment transport rate. Based on actual measurements of bottom shear stress, the mean bottom shear stress of test ST400a_ce increases the ratio τ_{bm+}/τ_{bm-} from 1.54 to 1.75, which means that the difference between the two maxima is increased by roughly 40 %. As a rule of thumb, the bedload sediment transport rate is proportional to the magnitude of bottom shear stress to the power of 3/2, so the net bedload sediment transport rate is roughly proportional to a period-averaged

quantity I_{BS} defined as

$$I_{BS} = \overline{|\tau_b(t)|^{3/2} \frac{\tau_b(t)}{|\tau_b(t)|}}, \tag{5.3}$$

where the overbar indicates period average. For Stokes-wave tests in this study, I_{BS} can be increased by roughly 50 % if the mean bottom shear stress is added to the total bottom shear stress. Therefore, it is possible that half of the measured net sediment transport rates under Stokes waves in OWTs is due to a facility-produced return current, which must be considered when deriving or validating empirical sediment transport formulae using OWT measurements.

5.3. *Currents in the presence of sinusoidal waves*

Comparisons of the measured and predicted current velocity profiles for six representative sinusoidal-wave–current tests are shown in figure 18. These tests are all with the SP400a wave (the strongest sinusoidal wave) but have different current and bottom conditions. The predictions given by the improved GM model (indicated by the dashed lines) are also provided. It should be noted that this model was derived with a three-layer turbulent eddy viscosity, but the predicted current velocity profile was further simplified by neglecting the smooth transition layer between the two logarithmic layers, so the curves have a sharp kink which we shall not consider when evaluating this model's performance. Generally speaking, the present model very accurately predicts the upper current profiles, while the accuracy deteriorates slightly in the very near-bottom region. The test SP400a_C13_ce shown in figure 18(*a*) has the worst agreement between measurements and predictions. This is possibly because it suffers from the most significant effect of the mean pressure gradient, since it has the largest apparent roughness (see discussions in § 3.1.1). The predictions given by the improved GM model closely follow the predictions of the present model. The predicted and measured current shear velocities are compared in figure 19. The present model generally overestimates the current shear velocity by approximately $6.1\,\% \pm 2.7\,\%$, while the improved GM model has a slightly better performance, i.e. the overestimate is $3.3\,\% \pm 6.1\,\%$. Thus, we conclude that both models accurately predict the current shear velocity.

Despite their equally good performance, the two models differ substantially in their formulation of the effect of waves on currents. For the GM-type model, only the basic wave–current interaction is considered, i.e. the waves influence the coexisting currents by increasing the turbulent eddy viscosity in the very near-bottom region. However, for the present model, the total current velocity is the sum of a basic current velocity $\bar{u}_c$ and a TA-streaming $\bar{u}_s$. In the very near-bottom region, $\bar{u}_c$ is controlled by a turbulent eddy viscosity which is scaled by the mean shear velocity $\bar{u}_*$, which is generally larger than u_{*c}, so the effect of an enhanced turbulent eddy viscosity still exist. However, it is weaker than that suggested by the GM model, since $\bar{u}_*$ is less than u_{*m}, which is used in the GM model to scale the mean bottom turbulent eddy viscosity, by a factor of roughly $\sqrt{2/\pi} = 0.8$ (assuming a weak current and a strong sinusoidal wave). Therefore, it is the existence of the TA-streaming, $\bar{u}_s$, which is entirely neglected in the improved GM model, that makes the GM model's predictions agree with those obtained from the present model. To illustrate this, the total current velocity $\bar{u}$ predicted by the present model is decomposed into $\bar{u}_c$ and $\bar{u}_s$. For simplicity, the following discussion is based on a representative test SP400a_C40_sa (figure 18*d*) which has the best agreement between model predictions and measurements.

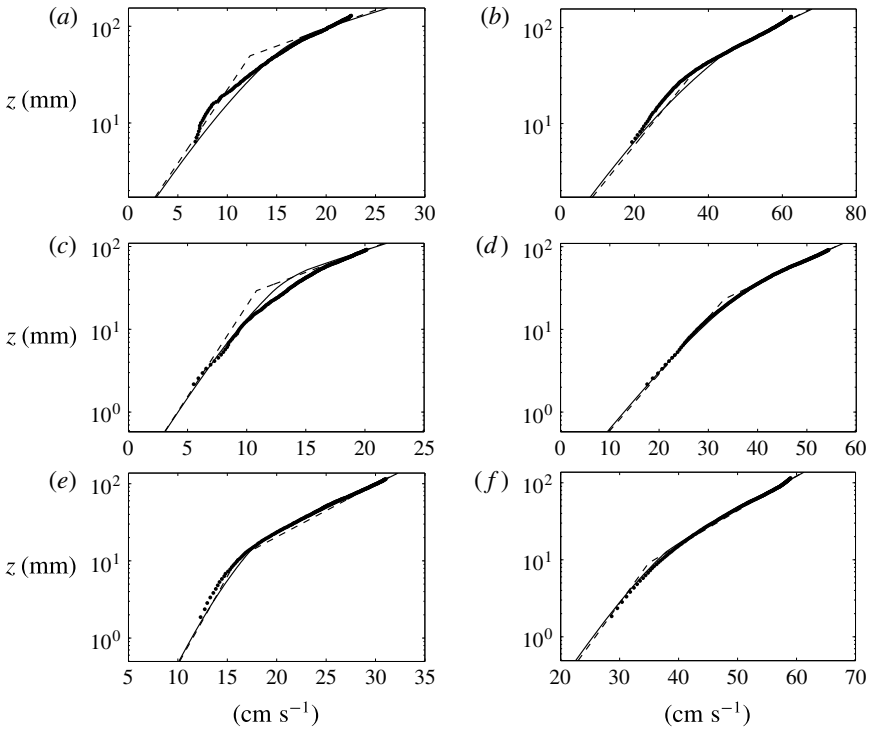

FIGURE 18. Prediction of current velocity profiles in the presence of sinusoidal waves (solid lines: the present model; dashed lines: the improved GM model; dots: measurements): (*a*) SP400a_C13_ce; (*b*) SP400a_C40_ce; (*c*) SP400a_c13_sa; (*d*) SP400a_c40_sa; (*e*) SP400a_c13_sm; (*f*) SP400a_c40_sm.

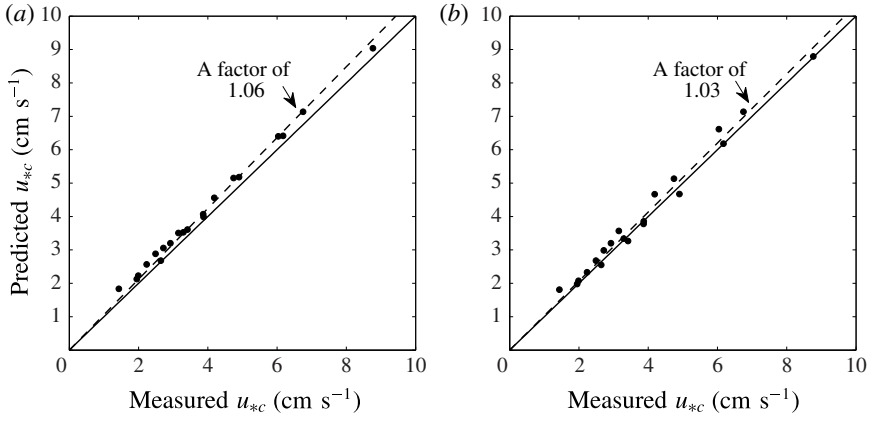

FIGURE 19. Comparison of the predicted and measured current shear velocity (solid line: perfect agreement; dashed lines: least-square fit to the data): (*a*) present model; (*b*) the improved GM model.

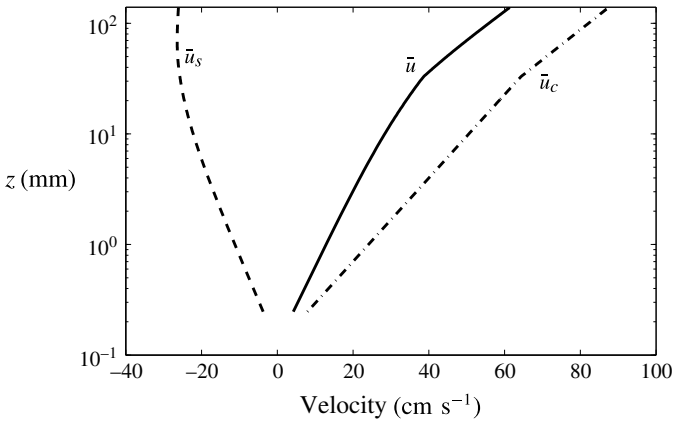

FIGURE 20. Decomposing of the total current velocity profile of test SP400a_C40_sa into a boundary layer streaming and a basic current velocity (solid line: total mean velocity; dashed line: boundary layer streaming; dash-dot line: basic current).

As shown in figure 20, the predicted $\bar{u}_s$ is opposing $\bar{u}_c$, and its magnitude is roughly a quarter of $\bar{u}_c$ at the level $z = 100$ mm, so it is a non-negligible component of the total current velocity profile. For sinusoidal-wave–current flows, $\bar{u}_s$ is mainly due to the interaction of the first-harmonic turbulent eddy viscosity and the first-harmonic velocity gradient. Thus, $\bar{u}_s$ can be roughly written as

$$\bar{u}_s(z) \approx \mathrm{Re}\left\{-\tfrac{1}{2}a_1 \mathrm{e}^{-\mathrm{i}\psi_1} u^{(1)}(z)\right\}. \tag{5.4}$$

For a superimposed basic current $\bar{u}_c$ in the positive direction, model predictions suggest that ψ_1 is always close to zero. The phase of $u^{(1)}(z)$, as suggested by measurements, changes by no more than 25° over the entire boundary layer. Thus, $\bar{u}_s$ can be further approximated as

$$\bar{u}_s(z) \approx -\tfrac{1}{2}a_1 |u^{(1)}(z)|. \tag{5.5}$$

This suggests that $\bar{u}_s$ is in the negative direction for a positive $\bar{u}_c$. For a negative $\bar{u}_c$, it can be easily proved that ψ_1 is changed to roughly $-180°$, so $\bar{u}_s$ becomes positive. Therefore, the TA-streaming embedded in the sinusoidal-wave–current flows is always against the direction of the superimposed current. In the very-near bottom region, the amplitude of the first-harmonic velocity $|u^{(1)}(z)|$ follows a logarithmic profile approximately controlled by the maximum wave shear velocity u_{*wm}, so the total mean velocity $\bar{u}$ can be written as

$$\bar{u}(z) = \bar{u}_c + \bar{u}_s = \frac{1}{\kappa}\left(-\frac{1}{2}a_1 u_{*wm} + \frac{{u_{*c}}^2}{\bar{u}_*}\right)\ln\left(\frac{z}{z_0}\right). \tag{5.6}$$

This suggests that $\bar{u}(z)$ is still logarithmic in the very near-bottom region. The shear velocity of the basic current velocity profile, $u_{*c}^2/\bar{u}_*$, is reduced by $a_1 u_{*wm}/2$, which corresponds to the effect of the TA-streaming. Thus, an 'effective' shear velocity is given by

$$u_{*c,a} = -\frac{1}{2}a_1 u_{*wm} + \frac{{u_{*c}}^2}{\bar{u}_*}. \tag{5.7}$$

In the GM-type models, the effective shear velocity for the lower current velocity profile is $u_{*c,b} = u_{*c}^2/u_{*m}$. For a simple yet realistic approximation, the bottom shear stress of the sinusoidal-wave–current flows can be taken as the sum of a sinusoidal wave bottom shear stress and a current bottom shear stress. With this approximation, we can evaluate the difference between $u_{*c,a}$ and $u_{*c,b}$ for various current conditions specified by u_{*c}/u_{*wm}. The results suggest that the ratio $u_{*c,a}/u_{*c,b}$ is between 0.93 and 1.15 for u_{*c}/u_{*wm} from 0 to 2 (very weak to very strong current). This explains why the two models give virtually identical predictions for the lower current velocity profile. Thus, by using u_{*m} as the scaling shear velocity, the GM model implicitly includes the effect of the TA-streaming which can only be predicted with a time-varying turbulent eddy viscosity.

5.4. *Currents in the presence of nonlinear waves*

For currents in the presence of nonlinear waves, both the wave nonlinearity and the current can produce TA-streaming, so the total $\bar{u}_s$ is the sum of two components: a current-related TA-streaming $\bar{u}_{sc}$, which is always against the current direction; and a wave-related TA-streaming $\bar{u}_{sw}$, which always opposes the wave direction. Therefore, $\bar{u}_{sw}$ and $\bar{u}_{sc}$ are co-directional for currents following nonlinear waves, resulting in an enhanced $\bar{u}_s$ that opposes currents. However, $\bar{u}_{sw}$ and $\bar{u}_{sc}$ are against each other for currents opposing nonlinear waves, resulting in a reduced $\bar{u}_s$ in the direction of the stronger of $\bar{u}_{sw}$ and $\bar{u}_{sc}$. For a given working frequency of the WCS pump, the total net volume discharge is maintained, so if added to a nonlinear wave, the basic current $\bar{u}_c$ of a positive current should be stronger (in terms of $|u_{*c}|$) than that of a negative current with the same pump frequency, so the difference in $\bar{u}_s$ is compensated. This explains why the vertical profiles of the total mean velocity $\bar{u}$ depend on current direction (e.g. see figure 9).

Figures 21 and 22 compare the model's predictions with the measurements for the four typical tests shown in figure 9, i.e. C13 currents (roughly 15 cm s^{-1} cross-section average velocity) and C40 currents (roughly 46 cm s^{-1} cross-section average velocity) following and opposing the strongest Stokes waves ST400a (first-harmonic velocity amplitude of 160 cm s^{-1} and 6.25 s wave period) over the sandpaper bottom. The model accurately predicts the mean velocity profiles for all four tests. For the two tests with the C40 current shown in figure 22, the predictions are in excellent agreement with the measurements. For test ST400a_C13_sa (figure 21*a*), the model reasonably predicts the very steep slope in the very near-bottom region, but the transition to the upper current profile takes place above the observed level. For test ST400a_C13r_sa (figure 21*c*), the current velocity profile does not have the conventional two-log-profile structure suggested by the GM model. The model successfully predicts this current velocity profile and offers a clear explanation for this phenomenon. As shown in figure 21(*d*), the two-log-profile structure is predicted for the basic current profile, but it is totally obliterated by the coexisting TA-streaming which is much stronger than the basic current.

The predicted current velocity profile for each test is also decomposed into $\bar{u}_c$ and $\bar{u}_s$. The two components of $\bar{u}_s$, $\bar{u}_{sc}$ and $\bar{u}_{sw}$, cannot be further isolated, but their mutual interaction can still be traced. Here we used the $\bar{u}_s$ for a pure Stokes wave ST400a_sa over the sandpaper bottom as a rough estimate of $\bar{u}_{sw}$. Figure 16 shows that $\bar{u}_{sw}$ is negative and its magnitude can reach the order of -20 cm s^{-1} at $z = 100$ mm. For a positive superimposed C13 current, $\bar{u}_{sw}$ enhances the co-directional $\bar{u}_{sc}$, so a sizeable total $\bar{u}_s$ opposing the current is produced, i.e. $\bar{u}_s$ is approximately -30 cm s^{-1} at $z = 100$ mm, as shown in figure 21(*b*). However, a negative superimposed C13

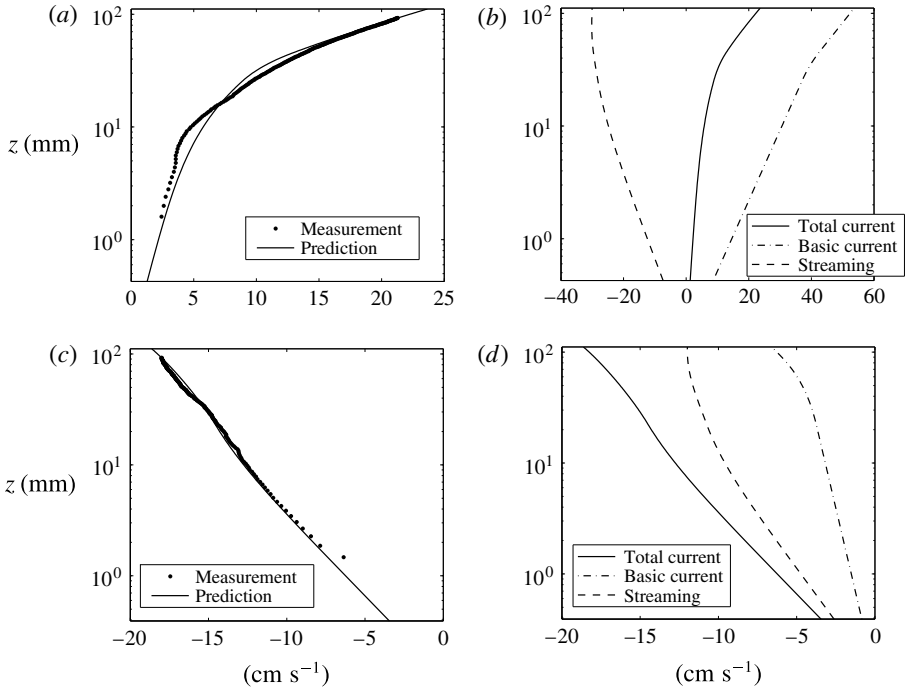

FIGURE 21. Predicted and measured current velocity profile of a C13 current following and opposing the ST400a wave over the sandpaper bottom: (*a*) predicted and measured current velocity profiles for ST400a_C13_sa, (*b*) decomposition of the predicted current velocity profile for test ST400a_C13_sa, (*c*) predicted and measured current velocity profiles for ST400a_C13r_sa, (*d*) decomposition of the predicted current velocity profile for test ST400a_C13r_sa.

current gives a positive $\bar{u}_{sc}$ opposing $\bar{u}_{sw}$, so the total $\bar{u}_s$ is the difference between its two components. As shown in figure 21(*d*), $\bar{u}_s$ is only -12 cm s^{-1} at $z = 100$ mm, and it follows the current, indicating that $\bar{u}_{sw}$ is stronger than $\bar{u}_{sc}$. Since the pump maintains a constant and preset discharge, the facility has to develop an additional current to cope with the different net discharges due to TA-streaming, which is analogous to the facility-generated return current balancing the TA-streaming for pure nonlinear wave tests. Therefore, the basic currents in the two tests are significantly different. A strong basic current is predicted for the test with a positive C13 current, i.e. $\bar{u}_c$ at $z = 100$ mm is over 50 cm s^{-1} in figure 21(*b*), but a much weaker basic current is required for the test with a negative C13 current, i.e. $\bar{u}_c$ is only -6 cm s^{-1} in figure 21(*d*).

The two tests with C40 currents give the same conclusions. For test ST400a_C40r_sa (figure 22*d*), the positive $\bar{u}_{sc}$ is slightly stronger than the negative $\bar{u}_{sw}$, so the total $\bar{u}_s$ is still against the current, but its magnitude (<6 cm s^{-1} at $z = 100$ mm) is much smaller than that of test ST400a_C40_sa (figure 22*b*) which is over -50 cm s^{-1} at $z = 100$ mm. Accordingly, a strong basic current, i.e. $u_c = 100$ cm s^{-1} at $z = 100$ mm, is predicted for test ST400a_C40_sa, while the basic current is much weaker for test ST400a_C40r_sa, i.e. u_c is only -65 cm s^{-1} at $z = 100$ mm.

Since the current (mean) bottom shear stress is only related to the basic current, the significant difference in the basic current velocity implies that the currents

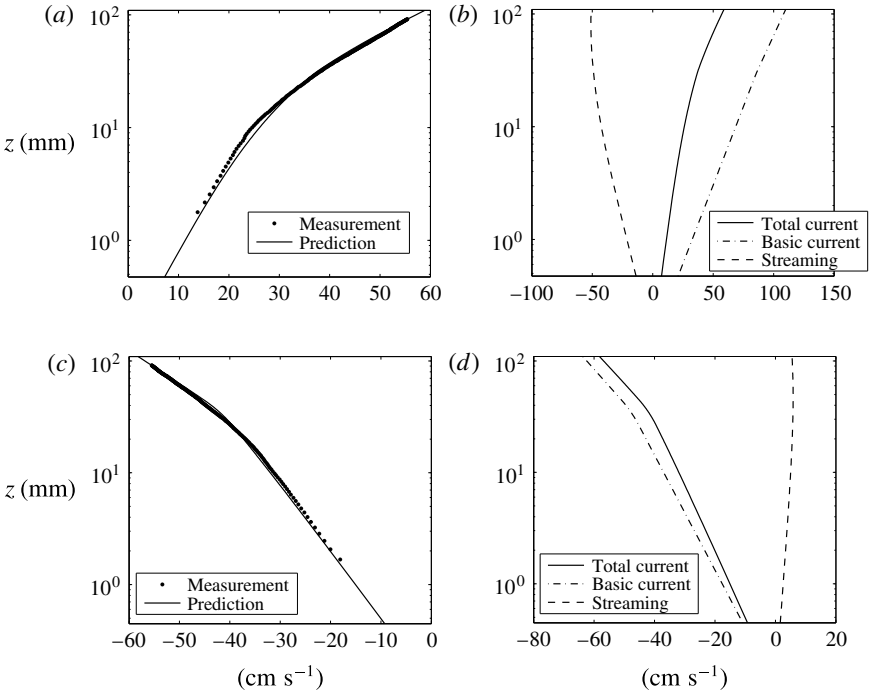

FIGURE 22. Predicted and measured current velocity profile of a C40 current following and opposing the ST400a wave over the sandpaper bottom: (*a*) predicted and measured current velocity profiles for ST400a_C40_sa, (*b*) decomposition of the predicted current velocity profile for test ST400a_C40_sa, (*c*) predicted and measured current velocity profiles for ST400a_C40r_sa, (*d*) decomposition of the predicted current velocity profile for test ST400a_C40r_sa.

following and opposing a nonlinear wave in the WCS are not comparable, despite the total mean discharge being the same. Another way to look at this implication is as follows. If we only use a target current velocity at a certain reference level or a total current discharge to specify a current, we cannot distinguish between boundary layer streaming and basic current, so such a specification of currents is inappropriate when the current bottom shear stress is the primary concern. In such situations, we suggest using the current bottom shear stress or the slope of the current velocity profile outside the wave boundary layer (see (B 8)) to specify currents, although this may make the experimental procedure more tedious.

We can validate the prediction of the basic current using the measured current bottom shear stress, since appendix B shows that the total current bottom shear stress is just the mean bottom shear stress given by the basic current. This can also indirectly validate the prediction of TA-streaming given that the total current velocity is accurately predicted. As shown in table 4, except for test ST400a_C13r_sa which has a very small u_{*c} and consequently a large relative error, the predicted u_{*c} is in excellent agreement with the measurements, i.e. the relative error for the remaining three tests is only approximately 5 % (overestimate), which is in agreement with the 6 % overestimate for the u_{*c} of sinusoidal-wave–current tests (figure 19). Both measurements and predictions suggest significant differences between the current shear velocities for currents following and opposing nonlinear waves, i.e.

Test ID	Measured u_{*c} (cm s^{-1})	Predicted u_{*c} (cm s^{-1})	Prediction/measurement (%)
ST400a_C13_sa	4.75	4.97	104.6
ST400a_C13r_sa	−1.10	−1.62	145.5
ST400a_C40_sa	7.11	7.48	105.2
ST400a_C40r_sa	−5.36	−5.69	106.1

TABLE 4. Predicted and measured current shear velocities for nonlinear-wave–current tests.

the experimental u_{*c} in test ST400a_C13_sa is more than four times larger than that of ST400a_C13r_sa in magnitude. Therefore, the present model not only reasonably predicts the total current velocity profile, but also accurately predicts its two components. If the improved GM model is applied to these tests, very similar values for u_{*c} will be predicted for following and opposing currents with the same pump setting, since the model does not consider the TA-streaming associated with the wave nonlinearity. Using approximated current velocities at $z = 100$ mm (20 cm s^{-1} and 55 cm s^{-1} for C13 and C40 currents, respectively) for specifying the current condition, the current shear velocities given by the improved GM model are 3.27 cm s^{-1} and 6.26 cm s^{-1} for tests with C13 and C40 currents, respectively. Therefore, u_{*c} will be dramatically overpredicted for the opposing currents, e.g. a factor of 3 for test ST400a_C13r_sa, but dramatically underpredicted for the following currents, e.g. 31 % for test ST400a_C13_sa. This shows that a GM-type model is not applicable in shallow waters where waves can be highly nonlinear.

These results also have important implications in the study of sediment transport under nonlinear-wave–current flows in OWTs. Since both the nonlinear wave and the current depend on direction, it is natural to compare the net sediment transports of currents following and opposing the nonlinear wave. If the total current discharge or a reference current velocity at a reference elevation is used to specify the current condition, the two basic currents obtained are not equivalent, i.e. the magnitudes of the current bottom shear stresses are not the same. Consequently, the two net sediment transports are not comparable. In such cases, the correct thing to do is to adjust the total current discharge to maintain the same magnitude of current bottom shear stress.

6. Conclusions

A high-quality experimental study including a large number of tests which correspond to full-scale coastal boundary layer flows is performed using a state-of-the-art OWT for flow generation and a PIV system for velocity measurements. The tests include three wave shapes, i.e. sinusoidal, Stokes and forward-leaning waves, combined with collinear currents over three different bottom roughness configurations: smooth, ‘sandpaper’ and ceramic-marble bottoms. For sinusoidal-wave–current flows, the typical two-log-profile structure of the current velocity profile suggested by the GM model is observed. The measured maximum wave bottom shear stress generalized in terms of the wave friction factor and the associated phase lead is reasonably predicted by the improved GM model developed by Humbyrd (2012). For the nonlinear-wave–current boundary layer flows, measurements from typical tests indicate that there is a substantial difference between currents of the same total discharge but opposing directions in the presence of nonlinear waves. For a weak current opposing a nonlinear wave, the two-log-profile structure suggested by the GM model may even be totally absent. This is because the wave-induced

turbulence asymmetry (TA) streaming contaminates the conventional two-log-profile structure. Therefore, the GM model is not able to predict the current profile for nonlinear-wave–current flows.

A semi-analytical model for oscillatory turbulent boundary layers is developed to interpret the experimental results. This model assumes that the flow is homogeneous in the wave direction and only considers a collinear superimposed current, so it is perfectly suitable for predicting boundary layer flows in OWTs. Following Trowbridge & Madsen (1984*a*,*b*) and Gonzalez-Rodriguez & Madsen (2011), the turbulent eddy viscosity is considered time-varying, and is expressed as the product of a temporal variation function and the mean turbulent eddy viscosity. Following Lavelle & Mofjeld (1983), a new temporal variable is introduced for easy decoupling and analytical solution of the wave and current equations. The backward conversion of the temporal variable and the closure hypothesis are obtained by numerical Fourier analyses. This semi-analytical model can not only achieve high model accuracy, but also decompose predictions of velocity and bottom shear stress into components with different physical origins. This is not easily achievable for completely numerical models, e.g. no previous numerical study cited in this paper has identified the turbulence asymmetry streaming for currents in the presence of sinusoidal waves. Therefore, this semi-analytical model is ideally suited for the purpose of this study, i.e. improving our physical understanding of boundary layer flows in OWTs.

For pure wave flows in OWTs, the model accurately predicts the dominant harmonics of oscillatory velocity, e.g. the first-harmonic velocity for both sinusoidal and nonlinear waves and the second-harmonic velocity for the nonlinear waves, while the smaller higher harmonics, e.g. the third-harmonic velocity, are only qualitatively predicted. The predictions of the bottom shear stress under pure wave flows are in excellent agreement with measurements obtained from log-profile fitting instantaneous velocity profiles.

Model prediction illustrates that the mean velocity embedded in nonlinear waves in OWTs is actually the difference between the wave-produced TA-streaming and a facility-produced return current necessary to maintain a zero net discharge. For certain wave shapes, both of these components can have magnitudes much stronger than the observed total mean velocity. The mean bottom shear stress is solely produced by the return current, and it can contribute significantly to the net sediment transport rates under nonlinear waves in OWTs. This must be realized when using OWT measurements to derive or validate empirical sediment transport formulae.

For currents in the presence of sinusoidal waves, both the present model and the improved GM model give good predictions of the current velocity profiles and the current bottom shear stress. However, there are substantial differences between the two models' formulations of the effect of waves on currents. For GM-type models, the waves influence the coexisting currents by increasing the turbulent eddy viscosity inside the wave boundary layer. This effect is relatively weaker in the present model, but another effect, the current-produced TA-streaming which is entirely missed in GM-type models, is added. It acts to retard the magnitude of the superimposed current in much the same manner as does an artificially increased turbulent eddy viscosity. Therefore, the present model and the improved GM model give nearly identical predictions of current velocity profiles, indicating that the GM model formulation implicitly accounts for the TA-streaming.

For currents in the presence of nonlinear waves, the present model successfully predicts the current velocity profiles and captures the difference between currents following and opposing the waves. The prediction illustrates that the TA-streaming,

which is due to the combined effect of the superimposed current and the wave nonlinearities, can significantly contaminate the basic current which follows the two-log-profile structure suggested by the GM model. In certain situations, such as a weak current in the opposite direction to a strong Stokes wave, the conventional two-log-profile structures is completely obliterated. This shows that it can be misleading to use the GM model for analysis of field measurements obtained in relatively shallow waters where the waves are nonlinear.

With the results presented in this paper, we have developed a thorough understanding of the boundary layer flows in OWTs, which is the prerequisite for interpreting OWT results on sediment transport rates. However, the effect of wave propagation, e.g. the Longuet-Higgins-type streaming, is completely absent for OWT flows, but can significantly affect both turbulent boundary layer flows and sediment transport rates in coastal waters, as suggested by many previous studies (e.g. Yu, Hsu & Hanes 2010; Fuhrman, Schløer & Sterner 2013; Holmedal *et al.* 2013; Kranenburg *et al.* 2013). Thus, it is inappropriate to blindly apply OWT results on hydrodynamics and sediment transport rates to the coastal environment. The correct methodology would be to first develop a good hydrodynamic model specifically for OWTs, such as the semi-analytical model of this study, and then based on this model develop a sediment transport model which is validated against OWT experiments. In this way, we gain confidence in the sediment transport model and can in due course extend the hydrodynamic model to progressive waves and couple it with the verified sediment transport model to obtain predictions for sediment transport rates in coastal waters. The extended model, of course, can also be validated against large-scale wave flume experiments (e.g. Dohmen-Janssen 2002). However, we want to point out that it is impractical to take large-flume experiments as the starting point, since their experimental costs are much higher, as reflected by the small quantity of reported studies so far, and their experimental conditions are much less controllable, e.g. it is very difficult to accurately generate sinusoidal waves with large amplitudes in wave flumes.

Acknowledgements

We gratefully acknowledge the financial support for this research from the National Research Foundation of Singapore (NRF) through the Singapore–MIT Alliance for Research and Technology's (SMART) Center for Environmental Sensing and Modeling (CENSAM) program. We also acknowledge the assistance from Professor C. E. Soon of the National University of Singapore (NUS) in obtaining space for the WCS facility in the Hydraulic Engineering Laboratory of the Civil and Environmental Engineering Department at the NUS.

Appendix A. Modification of the Grant–Madsen model

Humbyrd (2012) proposed the following continuous three-layer turbulent eddy viscosity:

$$\nu_t = \begin{cases} \kappa u_{*m} z, & z_0 < z \leqslant \delta_t, \\ \kappa u_{*m} \delta_t, & \delta_t < z \leqslant \delta_{ct}, \\ \kappa u_{*c} z, & \delta_{ct} < z. \end{cases} \tag{A 1}$$

Inside the wave boundary layer, ν_t is scaled with u_{*m} (the maximum shear velocity) but has a linear-constant structure, which gives the lowest two layers. The transition level δ_t is

$$\delta_t = \tfrac{1}{6}\delta_w, \tag{A 2}$$

where the wave boundary layer thickness δ_w is defined as the level where the wave velocity deficit reaches 5 % of the free-stream value and is obtained by iteratively solving the linearized boundary layer equation. Humbyrd gives an approximate explicit formula for δ_w/l:

$$\frac{\delta_w}{l} = \exp\left\{a\left(C_\mu \frac{A_{bm}}{k_b}\right)^b + c\right\}, \tag{A 3}$$

where l is a characteristic boundary layer length scale $l = \kappa u_{*m}/\omega$ and C_μ is the ratio of the maximum combined bottom shear stress τ_{bm} to the maximum wave bottom shear stress τ_{wm} which can be given in terms of $\alpha = u_{*c}/u_{*m}$:

$$C_\mu = (1-\alpha^2)^{-1}. \tag{A 4}$$

The parameters a, b, and c in (A 3) are also functions of α:

$$\begin{aligned} a &= \begin{cases} 2.03, & 0 < \alpha \leqslant 1/6, \\ -3.81\alpha^3 + 0.795\alpha^2 + 0.831\alpha + 1.92, & 1/6 < \alpha \leqslant 1, \end{cases} \\ b &= \begin{cases} -0.0849, & 0 < \alpha \leqslant 1/6, \\ a/(9.84\alpha^3 - 25.5\alpha^2 - 8.77\alpha - 22.6), & 1/6 < \alpha \leqslant 1, \end{cases} \\ c &= \begin{cases} -0.845, & 0 < \alpha \leqslant 1/6, \\ X_{\mu,crit}(-17.4\alpha^3 + 6.96\alpha^2 - 5.40\alpha - 1.77), & 1/6 < \alpha \leqslant 1, \end{cases} \end{aligned} \tag{A 5}$$

where

$$X_{\mu,crit} = \begin{cases} 0.342, & 0 \leqslant \alpha \leqslant 0.15, \\ 22.6\alpha^3 - 18.9\alpha^2 + 4.83\alpha - 0.035, & 0.15 \leqslant \alpha \leqslant 0.3, \\ 0.222\alpha^2 - 0.619\alpha + 0.490, & 0.3 \leqslant \alpha \leqslant 1. \end{cases} \tag{A 6}$$

The turbulent eddy viscosity associated with the current has a linear variation which will always intersect with the constant layer at a transition level:

$$\delta_{ct} = \delta_t/\alpha. \tag{A 7}$$

Since the current-generated turbulence becomes dominant above this level, ν_t is given by $\nu_t = \kappa u_{*c} z$, and hence the upper logarithmic layer of the current velocity profile starts from δ_{ct}.

With the three-layer turbulent eddy viscosity introduced above, the following solution of the current velocity profile is obtained:

$$\bar{u}(z) = \begin{cases} \dfrac{{u_{*c}}^2}{\kappa u_{*m}} \ln\left(\dfrac{z}{z_0}\right), & z_0 < z \leqslant \delta_t, \\ \dfrac{{u_{*c}}^2}{\kappa u_{*m}} \left[\dfrac{z-\delta_t}{\delta_t} + \ln\left(\dfrac{\delta_{ct}}{z_0}\right)\right], & \delta_t < z \leqslant \delta_{ct}, \\ \dfrac{u_{*c}}{\kappa}\left[\ln\left(\dfrac{z}{\delta_{ct}}\right) + 1 + \dfrac{u_{*c}}{u_{*m}}\left(\ln\left(\dfrac{\delta_t}{z_0}\right) - 1\right)\right], & \delta_{ct} < z. \end{cases} \tag{A 8}$$

The analytical solution of the wave velocity is not presented here for simplicity, and the reader is referred to Humbyrd (2012) for details. It should be noted that the wave amplitude profile follows the logarithmic law in the very near-bottom region, as suggested by (3.3).

Appendix B. Analytical solution for the current velocity

The current velocity $\bar{u}(z)$ is the sum of the solution of the current equation in τ-space, i.e. (4.24), and a mean velocity, $\bar{u}_V(z)$, produced when converting the wave solution from τ-space to t-space, which essentially represents the origin of the TA-streaming. After matching the no-slip boundary condition, $\bar{u}(z)$ is given by

$$\bar{u}(z) = \bar{u}_V(z) + \int_{z_0}^{z} \frac{c}{\bar{\nu}_t(z')} \mathrm{d}z' - \bar{u}_V(z_0). \tag{B 1}$$

The unknown constant c is obtained by matching the reference current velocity, and it can be shown to be the current bottom shear stress τ_{cb}/ρ as follows. We here consider the period average of the instantaneous bottom shear stress:

$$\frac{\tau_{cb}}{\rho} = \bar{\nu}_t(z_0)\overline{f(t)\frac{\partial(\tilde{u}+\bar{u}_V)}{\partial z}\bigg|_{z=z_0}} + c; \tag{B 2}$$

$(\tilde{u}+\bar{u}_V)$ is essentially the result of converting the oscillatory velocity from τ-space to t-space, so the first term on the right-hand side can be written in terms of the oscillatory velocity in τ-space as

$$\bar{\nu}_t(z_0)\overline{f(t)\frac{\partial(\tilde{u}+\bar{u}_V)}{\partial z}\bigg|_{z=z_0}} = \frac{\bar{\nu}_t(z_0)}{T}\left[\frac{\partial}{\partial z}\int_{\tau(0)}^{\tau(T)} \tilde{V}(z,\tau)\mathrm{d}\tau\right]\bigg|_{z=z_0}. \tag{B 3}$$

Here $f(t) = \mathrm{d}\tau/\mathrm{d}t$ is invoked. According to the definition of τ, $\tau(T) - \tau(0) = T$. Thus, the right-hand side of (B 3) contains an integral of a periodic function with a zero mean value over its period. Consequently, this term and hence the first term on the right-hand side of (B 2) are both zero, resulting in $c = \tau_{cb}/\rho$. Therefore, the current velocity profile is given by

$$\bar{u}(z) = \bar{u}_s(z) + \bar{u}_c(z), \tag{B 4}$$

where

$$\bar{u}_s(z) = \bar{u}_V(z) - \bar{u}_V(z_0) \tag{B 5}$$

and

$$\bar{u}_c(z) = \int_{z_0}^{z} \frac{\tau_{cb}/\rho}{\bar{\nu}_t(z')} \mathrm{d}z'. \tag{B 6}$$

The $\bar{u}_s(z)$ is produced by the interaction of the time-varying turbulent eddy viscosity and the time-varying velocity, so it represents the TA-streaming; $\bar{u}_c(z)$, however, carries no information about the temporal variation of the turbulent eddy viscosity, so it essentially represents the superimposed current, and will be referred as the 'basic current velocity'. With this separation of the mean velocity, we can divide the mean bottom shear stress into three parts:

$$\frac{\tau_{cb}}{\rho} = \left[\overline{\nu_t(z,t)\frac{\partial\tilde{u}}{\partial z}} + \bar{\nu}_t(z)\frac{\partial\bar{u}_s}{\partial z}\right]\bigg|_{z=z_0} + \bar{\nu}_t(z)\left.\frac{\partial\bar{u}_c}{\partial z}\right|_{z=z_0}. \tag{B 7}$$

The previous arguments demonstrate that the sum of the first two terms is zero, which suggests that the mean bottom shear stress related to the product of the time-varying

velocity gradient and the time-varying turbulent eddy viscosity (first term) is balanced by the mean bottom shear stress related to the TA-streaming (second term). Therefore, the wave alone will not produce a mean bottom shear stress, regardless of the wave shape. The reason for getting non-zero mean bottom shear stresses for nonlinear waves in the OWTs is the 'return current' required to have a zero net volume flux, which is equivalent to superimposing a current. Thus, the mean bottom shear stress is indeed the 'current' bottom shear stress. This gives us a consistent way to define the equivalence of currents in the presence of different waves: two equivalent superimposed currents have the same mean bottom shear stress. Using (4.15) for $\bar{\nu}_t$, the integral of $\bar{u}_c(z)$ can be analytically evaluated to give

$$\bar{u}_c(z) = \begin{cases} \dfrac{r_{wc}u_{*c}}{\kappa}\ln\left(\dfrac{z}{z_0}\right), & z_0 \leqslant z < \delta_I, \\ \dfrac{r_{wc}u_{*c}}{\kappa}\dfrac{z-\delta_I}{\delta_I} + \bar{u}_c(\delta_I), & \delta_I \leqslant z < \delta_J, \\ \dfrac{r_{wc}u_{*c}}{\kappa}\left[\dfrac{l}{\gamma\delta_I}(\mathrm{e}^{\gamma((z-\delta_J)/l)} - 1)\right] + \bar{u}_c(\delta_J), & \delta_J \leqslant z < \delta_K, \\ \dfrac{u_{*c}}{\kappa}\ln\left(\dfrac{z}{\delta_K}\right) + \bar{u}_c(\delta_k), & \delta_K \leqslant z, \end{cases} \tag{B 8}$$

where

$$r_{wc} = \frac{|u_{*c}|}{\bar{u}_*}. \tag{B 9}$$

It should be noted that the u_{*c} in (B 8) will be negative if τ_{cb} is in the negative direction. Its value is given by matching the reference current velocity:

$$\bar{u}(z_r, u_{*c}) = u_r. \tag{B 10}$$

After this, the current velocity is analytically obtained.

REFERENCES

VAN DER A, D. A., O'DONOGHUE, T., DAVIES, A. G. & RIBBERINK, J. S. 2011 Experimental study of the turbulent boundary layer in acceleration-skewed oscillatory flow. *J. Fluid Mech.* **684**, 251–283.

VAN DER A, D. A., O'DONOGHUE, T. & RIBBERINK, J. S. 2010 Measurements of sheet flow transport in acceleration-skewed oscillatory flow and comparison with practical formulations. *Coast. Engng* **57** (3), 331–342.

ARNSKOV, M.M., FREDSØE, J. & SUMER, B. M. 1993 Bed shear stress measurements over a smooth bed in three-dimensional wave-current motion. *Coast. Engng* **20** (3), 277–316.

BIJKER, E. W. 1966 The increase of bed shear in a current due to wave motion. *Coast. Engng Proc.* **1** (10), 749–765.

BLONDEAUX, P., VITTORI, G., BRUSCHI, A., LALLI, F. & PESARINO, V. 2012 Steady streaming and sediment transport at the bottom of sea waves. *J. Fluid Mech.* **697**, 115–149.

CHRISTOFFERSEN, J. B. & JONSSON, I. G. 1985 Bed friction and dissipation in a combined current and wave motion. *Ocean Engng* **12** (5), 387–423.

DAVIES, A. G. & LI, Z. 1997 Modelling sediment transport beneath regular symmetrical and asymmetrical waves above a plane bed. *Contin. Shelf Res.* **17** (5), 555–582.

DOHMEN-JANSSEN, C. M. 1999 Grain size influence on sediment transport in oscillatory sheet flow. Phase lags and mobile-bed effects. PhD thesis, Delft University of Technology.

DOHMEN-JANSSEN, C. M. & HANES, D. M. 2002 Sheet flow dynamics under monochromatic nonbreaking waves. *J. Geophys. Res.* **107** (C10), 3149.

VAN DOORN, TH. 1981 Experimental investigation of near-bottom velocities in water waves with and without a current. *Tech. Rep.* M1423, Delft Hydraulics.

DRAKE, D. E. & CACCHIONE, D. A. 1992 Wave-current interaction in the bottom boundary layer during storm and non-storm conditions: observations and model predictions. *Contin. Shelf Res.* **12** (12), 1331–1352.

DUNGAN SMITH, J. 1977 Modeling of sediment transport on continental shelves. *Sea* **6**, 539–577.

FERNANDO, P. C., GUO, J. & LIN, P. 2011 Wave-current interaction at an angle 1: experiment. *J. Hydraul. Res.* **49** (4), 424–436.

FREDSØE, J., ANDERSEN, K. H. & SUMER, B. M. 1999 Wave plus current over a ripple-covered bed. *Coast. Engng* **38** (4), 177–221.

FUHRMAN, D. R., FREDSØE, J. & SUMER, B. M. 2009 Bed slope effects on turbulent wave boundary layers. 2. Comparison with skewness, asymmetry, and other effects. *J. Geophys. Res.* **114** (C3), C03025.

FUHRMAN, D. R., SCHLØER, S. & STERNER, J. 2013 Rans-based simulation of turbulent wave boundary layer and sheet-flow sediment transport processes. *Coast. Engng* **73**, 151–166.

GONZALEZ-RODRIGUEZ, D. & MADSEN, O. S. 2011 Boundary-layer hydrodynamics and bedload sediment transport in oscillating water tunnels. *J. Fluid Mech.* **667**, 48–84.

GRANT, W. D. & MADSEN, O. S. 1979 Combined wave and current interaction with a rough bottom. *J. Geophys. Res.* **84** (C4), 1797–1808.

HOLMEDAL, L. E., JOHARI, J. & MYRHAUG, D. 2013 The seabed boundary layer beneath waves opposing and following a current. *Contin. Shelf Res.* **65**, 27–44.

HOLMEDAL, L. E. & MYRHAUG, D. 2006 Boundary layer flow and net sediment transport beneath asymmetrical waves. *Contin. Shelf Res.* **26** (2), 252–268.

HOLMEDAL, L. E. & MYRHAUG, D. 2009 Wave-induced steady streaming, mass transport and net sediment transport in rough turbulent ocean bottom boundary layers. *Contin. Shelf Res.* **29** (7), 911–926.

HUMBYRD, C. J. 2012 Turbulent combined wave-current boundary layer model for application in coastal waters. Master's thesis, Massachusetts Institute of Technology, Cambridge, MA, USA.

JENSEN, B. L., SUMER, B. M. & FREDSØE, J. 1989 Turbulent oscillatory boundary layers at high Reynolds numbers. *J. Fluid Mech.* **206**, 265–297.

JIMÉNEZ, J. 2004 Turbulent flows over rough walls. *Annu. Rev. Fluid Mech.* **36** (1), 173–196.

JONSSON, I. G. & CARLSEN, N. A. 1976 Experimental and theoretical investigations in an oscillatory turbulent boundary layer. *J. Hydraul. Res.* **14** (1), 45–60.

KEMP, P. H. & SIMONS, R. R. 1982 The interaction between waves and a turbulent current: waves propagating with the current. *J. Fluid Mech.* **116**, 227–250.

KEMP, P. H. & SIMONS, R. R. 1983 The interaction of waves and a turbulent current: waves propagating against the current. *J. Fluid Mech.* **130**, 73–89.

KRANENBURG, W. M., RIBBERINK, J. S., SCHRETLEN, J. J. L. M. & UITTENBOGAARD, R. E. 2013 Sand transport beneath waves: the role of progressive wave streaming and other free surface effects. *J. Geophys. Res.* **118** (1), 122–139.

KRANENBURG, W. M., RIBBERINK, J. S., UITTENBOGAARD, R. E. & HULSCHER, S. J. M. H. 2012 Net currents in the wave bottom boundary layer: on waveshape streaming and progressive wave streaming. *J. Geophys. Res.* **117**, F03005.

LAVELLE, J. W. & MOFJELD, H. O. 1983 Effects of time-varying viscosity on oscillatory turbulent channel flow. *J. Geophys. Res.* **88** (C12), 7607–7616.

LIM, K. Y., MADSEN, O. S. & CHEONG, H. F. 2012 Current characteristics in the presence of near-orthogonal waves. *Proceedings of the 33rd International Conference on Coastal Engineering*, p. currents. 41.

LODAHL, C. R., SUMER, B. M. & FREDSØE, J. 1998 Turbulent combined oscillatory flow and current in a pipe. *J. Fluid Mech.* **373**, 313–348.

LONGUET-HIGGINS, M. S. 1953 Mass transport in water waves. *Phil. Trans. R. Soc. Lond.* A **245** (903), 535–581.

MADSEN, O. S. 1994 Spectral wave-current bottom boundary layer flows. In *Proceedings of the 24th International Conference on Coastal Engineering*, pp. 384–398. ASCE.

MATHISEN, P. P. & MADSEN, O. S. 1996*a* Waves and currents over a fixed rippled bed. 1. Bottom roughness experienced by waves in the presence and absence of currents. *J. Geophys. Res.* **101** (C7), 16533–16542.

MATHISEN, P. P. & MADSEN, O. S. 1996*b* Waves and currents over a fixed rippled bed. 2. Bottom and apparent roughness experienced by currents in the presence of waves. *J. Geophys. Res.* **101** (C7), 16543–16550.

MATHISEN, P. P. & MADSEN, O. 1999 Waves and currents over a fixed rippled bed. 3. Bottom and apparent roughness for spectral waves and currents. *J. Geophys. Res.* **104** (C8), 18447–18461.

MUSUMECI, R., CAVALLARO, L., FOTI, E., SCANDURA, P. & BLONDEAUX, P. 2006 Waves plus currents crossing at a right angle: experimental investigation. *J. Geophys. Res.* **111**, C07019.

MYRHAUG, D. & SLAATTELID, O. H. 1989 Combined wave and current boundary layer model for fixed rough seabeds. *Ocean Engng* **16** (2), 119–142.

NIKURADSE, J. 1932 Gesetzmässigkeiten der turbulenten strömung in glatten rohren. *Ver. Dtsch. Ing. Forsch.* **3**, 1–36.

O'DONOGHUE, T. & WRIGHT, S. 2004 Flow tunnel measurements of velocities and sand flux in oscillatory sheet flow for well-sorted and graded sands. *Coast. Engng* **51**, 1163–1184.

RIBBERINK, J. S. & AL-SALEM, A. A. 1995 Sheet flow and suspension of sand in oscillatory boundary layers. *Coast. Engng* **25** (3–4), 205–225.

RUESSINK, B. G., MICHALLET, H., ABREU, T., SANCHO, F., VAN DER A, D. A., VAN DER WERF, J. J. & SILVA, P. A. 2011 Observations of velocities, sand concentrations, and fluxes under velocity-asymmetric oscillatory flows. *J. Geophys. Res.* **116**, C03004.

RUSSELL, R. C. H. & OSORIO, J. D. C. 1958 An experimental investigation of drift profiles in a closed channel. *Coast. Engng Proc.* **1** (6), 10.

SCANDURA, P. 2007 Steady streaming in a turbulent oscillating boundary layer. *J. Fluid Mech.* **571**, 265–280.

SLEATH, J. F. A. 1987 Turbulent oscillatory flow over rough beds. *J. Fluid Mech.* **182**, 369–409.

SLEATH, J. F. A. 1991 Velocities and shear stresses in wave-current flows. *J. Geophys. Res.* **96** (C8), 15237–15244.

TROWBRIDGE, J. & MADSEN, O. S. 1984*a* Turbulent wave boundary layers. 1. Model formulation and first-order solution. *J. Geophys. Res.* **89** (C5), 7989–7997.

TROWBRIDGE, J. & MADSEN, O. S. 1984*b* Turbulent wave boundary layers. 2. Second-order theory and mass transport. *J. Geophys. Res.* **89** (C5), 7999–8007.

WIJETUNGE, J. J. 2006 Velocity and turbulence distribution in combined oscillatory and steady flow boundary layer over a rippled bed. *Coast. Engng J.* **48** (03), 197–223.

YU, X., HSU, T. & HANES, D. M. 2010 Sediment transport under wave groups: relative importance between nonlinear waveshape and nonlinear boundary layer streaming. *J. Geophys. Res.* **115**, C02013.

YUAN, J. 2013 Experimental and theoretical study of turbulent oscillatory boundary layers. PhD thesis, Massachusetts Institute of Technology.

YUAN, J. & MADSEN, O. S. 2014 Experimental study of turbulent oscillatory boundary layers in an oscillating water tunnel. *Coast. Engng* **89**, 63–84.